



**HAL**  
open science

## Fault growth mechanisms and scaling properties in foreland basin system: The case study of Monte Alpi, Southern Apennines, Italy

Vincenzo La Bruna, Fabrizio Agosta, Juliette Lamarche, Sophie Viseur, Giacomo Prosser

### ► To cite this version:

Vincenzo La Bruna, Fabrizio Agosta, Juliette Lamarche, Sophie Viseur, Giacomo Prosser. Fault growth mechanisms and scaling properties in foreland basin system: The case study of Monte Alpi, Southern Apennines, Italy. *Journal of Structural Geology*, 2018, 116, pp.94-113. 10.1016/j.jsg.2018.08.009 . hal-02091081

**HAL Id: hal-02091081**

**<https://hal.science/hal-02091081v1>**

Submitted on 29 Nov 2022

**HAL** is a multi-disciplinary open access archive for the deposit and dissemination of scientific research documents, whether they are published or not. The documents may come from teaching and research institutions in France or abroad, or from public or private research centers.

L'archive ouverte pluridisciplinaire **HAL**, est destinée au dépôt et à la diffusion de documents scientifiques de niveau recherche, publiés ou non, émanant des établissements d'enseignement et de recherche français ou étrangers, des laboratoires publics ou privés.

1     **Fault growth mechanisms and scaling properties in foreland basin system: The case**  
2                                   **study of Monte Alpi, Southern Apennines, Italy**

3     **Vincenzo La Bruna<sup>1,2</sup>, Fabrizio Agosta<sup>2</sup>, Juliette Lamarche<sup>1</sup>, Sophie Viseur<sup>1</sup>, Giacomo**  
4                                   **Prosser<sup>2</sup>**

5  
6     <sup>1</sup>CEREGE-UMR 34, Aix-Marseille University, Marseille, France

7     <sup>2</sup>Department of Sciences, University of Basilicata, Italy

8  
9     Corresponding author: Vincenzo La Bruna (vincenzolabruna@gmail.com)

10  
11    **Key words:** syn-sedimentary faults, orthogonal fault system; fault dimensional properties,  
12    Apulian Platform, 3D geological reconstruction.

13  
14    **Abstract**

15    The present work focuses on the comprehension of the growth mechanisms and dimensional  
16    properties of the pre-Pliocene Monte Alpi fault network by mean of integrated field and  
17    laboratory analyses. After this multidisciplinary approach, detailed throw profiles are  
18    computed for each fault belonging to the Monte Alpi network. Subsequently, the dimensional  
19    properties of the individual faults are calculated. Data obtained from this work are discussed  
20    in terms of fault growth mechanisms and timing of deformation, and reported in a conceptual  
21    tectonic evolution model of the Messinian foreland basin system. Data suggest that originally  
22    isolated fault segments developed during the earliest stages of foreland basin formation by re-  
23    activation of a pre-existing, Early Cretaceous fault set, and formation of an orthogonal one.  
24    These two fault sets formed a scale-independent network. Differently, the same fault sets  
25    were also active during its subsequent development forming a scale-dependent fault network

26 characterized by T- and Y-shaped fault intersections. This deformation controlled the half-  
27 graben depocenters evolution filled by up to ca. 600 meters of terrigenous deposits during the  
28 Late Messinian time.

29

## 30 **1. Introduction**

31 Numerous studies have shed light on the evolution of the foreland basin systems flanking  
32 orogenic belts, but some gaps remain in particular related to the understanding of the fault  
33 growth mechanism and fault dimensional properties related to the structural networks that  
34 control the foreland basin system evolution. This knowledge is important to decipher the  
35 modalities of the extensional deformation associated to foreland flexure, which is commonly  
36 due to migration of Fold-and-Thrust belts (FTB), and unveil the possible role exerted by pre-  
37 existing, inherited faults on development of foreland basin systems (Gawthorpe and Leedert,  
38 2000). As documented in literature, longitudinal extensional faults parallel to the main thrust  
39 front of the FTB are frequently observed across the whole foreland basin system (Harding and  
40 Tuminas, 1989; Lorenzo et al., 1998; Ranero et al., 2003). Moreover, subordinated transverse  
41 extensional faults, which are perpendicular to the main thrust front can develop because of the  
42 stress release in the fault hanging wall of longitudinal faults (Destro, 1995; Medwedeff and  
43 Krantz 2002; Tavani et al., 2015), or be present as transfer faults within linked extensional  
44 systems (Tavarnelli et al., 1999).

45 Subsequently, during the migration of the orogenic chain this inner portion of the foreland  
46 basin system and its orthogonal fault network could experience orogenic compression and  
47 incorporated in FTBs.

48 In this paper, we present the results of a study performed in the Monte Alpi area which  
49 represent a key tectonic window of the southern Apennines FTB of Italy (Alberti et al., 2001;  
50 Patacca and Scandone, 2007). There, Mesozoic carbonates pertaining to the Inner Apulian

51 Platform (Sartoni and Crescenti, 1962) and overlapping Lower Messinian carbonates and  
52 Upper Messinian siliciclastic rocks (Sgrosso, 1988; Taddei and Siano, 1992) crop out in the  
53 axial portion of the belt (Cello and Mazzoli, 1998).

54 This peculiar site represents a unique opportunity to study and unveil the structural control  
55 exerted by an orthogonal fault network which controlled the evolution of the Messinian  
56 foreland basin system (Patacca et al., 1992), subsequently involved in several tectonic phases  
57 (Van Dijk et al., 2000; Mazzoli et al., 2006; La Bruna et al., 2017).

58 The results of this work may provide useful insights in order to better assess the timing of  
59 formation of the two aforementioned high-angle fault sets, which pre-date Early-Middle  
60 Pliocene contractional deformation associated to the FTB migration (Patacca and Scandone,  
61 2007). In particular, data obtained after a detailed field structural and stratigraphic analyses  
62 are employed, together with available subsurface data, to perform 3D geological  
63 reconstruction of a ca. 320 km<sup>2</sup> wide area. As a result, both attitude and cumulative throw  
64 profiles are computed for the individual, outcropping, high-angle faults crosscutting the  
65 Monte Alpi Unit. By also considering the displacement of specific chronostratigraphic  
66 surfaces, the dimensional properties of the evolving pre-Pliocene fault network are discussed  
67 in terms of either scale-independent (Schultz et al., 2008) or scale-dependent geometries (Kim  
68 and Sanderson, 2005). In fact, as described in literature, when initially isolated fault segments  
69 interact and, possibly, link together during ongoing deformation, they modify their  
70 dimensional properties (Walsh and Watterson, 1988; Peacock and Sanderson, 1991;  
71 Cartwright et al., 1995; Dawers and Anders, 1995; Mansfield and Cartwright, 1996; Crider  
72 and Pollard, 1998; Cowie and Roberts, 2001; Walsh et al., 2003). Considering the following  
73 relationship between the maximum fault cumulative displacement (D) and its maximum linear  
74 dimension (L, length)

$$75 \quad D=cL^n \quad \text{(eq. 1)}$$

76 where the  $c$  value is related to the rock mechanical properties, it is possible to assess the  
77 geometrical properties of the fault network by considering the  $n$  value (Watterson, 1986;  
78 Walsh and Watterson, 1988; Cowie and Scholz, 1992a,b; Scholz et al., 1993; Schlische et al.,  
79 1996; Kim and Sanderson, 2005; Schultz et al., 2008). Values of  $n=1$  indicate a linear scaling  
80 law (i.e. self-similarity), which implies that faults grew under conditions of constant driving  
81 stress at different scales, whereas values of  $n>1$  suggest a scale-dependent geometry.  
82 Regarding the study area of Monte Alpi, the contribution provided by the different angles  
83 among intersecting faults forming a scale dependent geometry is investigated by considering  
84 both T- and Y-shaped intersections (Maerten et al., 1999). Finally, evolution of the pre-  
85 Pliocene fault network is summarized in a conceptual model of Messinian foreland basin  
86 system evolution by taking the computed time-dependent activity of individual fault sets into  
87 account (sensu Gawthorpe and Leedert, 2000).

88

## 89 **2. Geological setting**

### 90 *2.1 Southern Apennines*

91 The Apennines are an arc-shaped FTB that formed in response to the Oligocene-to-Pliocene  
92 continental collision between Eurasian and African lithospheric plates (Royden et al., 1987;  
93 Locardi, 1988). Such a process caused the formation of east-propagating thrust sheets, which  
94 involved Meso-Cenozoic terranes originally pertaining to the Neo-Tethys Ocean, and of its  
95 south-eastern continental margin, and/or to the subduction-related accretionary wedge  
96 (Patacca et al., 1990; Doglioni, 1991). Commonly, the Apennines are sub-divided along-strike  
97 into three sectors named as northern, central, and southern, respectively, bounded by  
98 lithospheric discontinuities trending at high-angles with respect to the belt axis (Locardi,  
99 1988; Ghisetti and Vezzani, 1997; Vai and Martini, 2001; Cavazza et al., 2004; Patacca and  
100 Scandone, 2007). Most of the paleogeographic models proposed for the Mesozoic Neo-Tethys

101 ocean invoked two main carbonate platforms commonly identified as Apenninic, to the west,  
102 and Apulian, to the east, separated from each other by communicating basins (D'Argenio et  
103 al., 1972; Ippolito et al., 1975; Mostardini and Merlini, 1986; Tavarnelli and Prosser, 2003;  
104 Schettino and Turco, 2011).

105 The current structural setting of the southern Apennines FTB includes the following tectono-  
106 stratigraphic units, from the top to the bottom, which respectively correspond to specific  
107 paleogeographic domains arranged from west to east, respectively (Patacca and Scandone,  
108 2007): i) siltstones and claystones originally pertaining to the Liguride/Sicilide oceanic Basin;  
109 ii) carbonates derived from the Apennine Platform; iii) mixed terrigenous-carbonate rocks  
110 derived from the Lagonegro basin, divided into two different tectonic Units, Lagonegro I and  
111 II; and iv) carbonates of the Apulian Platform (Figure 1). Miocene-to-Pliocene terrigenous  
112 infill of foredeep, thrust-top, and piggyback basins were involved in contractional  
113 deformation, and currently crop out in the axial and outer portions of the belt (Ghisetti and  
114 Vezzani, 1981; Dewey et al., 1989; Boccaletti et al., 1990; Carbone et al., 1990; Van Dijk and  
115 Okkes, 1990, 1991; Monaco and Tanzi, 1992; Catalano et al., 1993; Monaco and Tortorici,  
116 1995; Monaco et al., 1998; Pescatore et al., 1999; Menardi Noguera and Rea, 2000; Patacca  
117 and Scandone, 2007). The Inner Apulian Platform was involved in Late Pliocene-Early  
118 Pleistocene thick-skinned tectonics (Mostardini and Merlini, 1986; Cello and Mazzoli, 1998;  
119 Butler et al., 2004; Shiner et al., 2004), whereas the Outer Apulian Platform is now days  
120 either exposed or buried underneath a Plio-Pleistocene sedimentary cover in the orogenic  
121 foreland of the Southern Apennines (Pieri et al., 1997; Borgomano, 2000; Spalluto, 2012;  
122 Panza et al., 2016; Petruccio et al., 2017). (insert Figure 1).

123

124 *2.2 Monte Alpi Unit*

125 The study area is located in the axial portion of the southern Apennines FTB (Figure 1). Over  
126 the years, according to the presumed age of the sedimentary cover, many authors proposed  
127 two conflicting hypotheses on the origin of the Monte Alpi carbonates. Assigning a Lower  
128 Miocene age to its sedimentary cover, the Mesozoic carbonates were interpreted as part of the  
129 Apennine Platform (Ogniben, 1969; Mostardini and Merlini, 1986; Muller et al., 1988).  
130 Differently, by assigning a Messinian age, other authors included them in the Inner Apulian  
131 Platform (Carbone et al., 1988; Sgrosso, 1988; Van Dijk et al., 2000; Alberti et al., 2001;  
132 Mazzoli et al., 2006, 2014). Structurally, the two most recent studies interpreted Monte Alpi  
133 as comprised of Apulian carbonates either forming a push-up structure (Van Dijk et al., 2000)  
134 or as the product of complex thin- and thick-skinned tectonics (Shiner et al., 2004; Mazzoli et  
135 al., 2006, 2014).

136 According to their inferred age of activity, La Bruna et al. (2017) recognized six different  
137 structural networks and documented two main sets of high-angle faults pre-dating Early-  
138 Middle Pliocene emplacement of the allochthon over the Mesozoic carbonates and their  
139 Upper Miocene cover (Cello and Mazzoli 1998; Buttler et al., 2004). The two high-angle fault  
140 sets formed an almost orthogonal fault system, which developed during either Cretaceous  
141 strike-slip and dip-slip tectonics (Pieri and Laviano, 1989; Festa et al., 2003; Mazzoli et al.,  
142 2006; Bertok et al., 2012; Tavani et al., 2013; Korneva et al., 2014; Panza et al., 2015, 2016;  
143 Laurita et al., 2016; Vitale et al., 2017), or Upper Miocene foreland bulging (Doglioni et al.,  
144 1995) and/or along-foredeep stretching (Tavani et al., 2015a).

145 The Monte Alpi Unit is made up of ca. 2,000 m-thick, Jurassic-to-Lower Cretaceous  
146 limestones and dolostones, and Messinian carbonates-terrigenous rocks (Figure 2). The  
147 Jurassic carbonates are Middle-to-Upper Jurassic in age, whereas the Lower Cretaceous ones  
148 are ascribed to the Neocomian (De Lorenzo, 1895; Selli, 1957; Sartoni and Crescenti, 1962;

149 Grandjacquet, 1963; Roda, 1965; Ogniben, 1969). The Messinian sedimentary succession is  
150 stacked into two main intervals (Sgrosso et al., 1988; Ortolani and Torre, 1971; Taddei and  
151 Siano, 1992; Van Dijk et al., 2000). The Lower Messinian deposits, which form a  
152 paraconformity with the Lower Cretaceous carbonates, consist of up to 35 m-thick skeletal  
153 grainstones and minor packstones, floatstones, rudstones and bindstones. Differently, the  
154 Upper Messinian deposits, which form a 3° to 5° angular unconformity with both Lower  
155 Messinian and Lower Cretaceous carbonates, include polygenic conglomerates, litharenitic  
156 sandstones, and siltstones characterized by remarkable thickness and compositional  
157 variations. (insert Figure 2).

158

### 159 **3. Data and Methods**

160 The proposed integrated approach includes a variety of methods such as geological mapping,  
161 field structural and stratigraphic analyses, well log correlation, seismic profile interpretation,  
162 and 3D surfaces reconstruction.

#### 163 *3.1 Field analysis*

164 The large-scale geological map was compiled at a 1:25,000 scale (Figure 2) by taking into  
165 account available published data (Foglio IGM 211, S. Arcangelo; Bonardi et al., 2009;  
166 Cavalcante et al., 2009; Lentini, 1991), and the detailed geological map originally compiled at  
167 a 1:10,000 scale by La Bruna et al. (2017). Field structural analyses focused on the fault zones  
168 exposed in the Monte Alpi area. Eight stratigraphic logs were measured in key sites, which  
169 expose significant portions of the Lower and Upper Messinian deposits.

170

#### 171 *3.2 Seismic profile interpretation*

172 Interpretation of the four stacked seismic reflection profiles (courtesy of Eni) was aimed at  
173 deciphering the geometry of the buried Apulian carbonates (Figure 3). Due to the general

174 poor quality of the seismic profiles, such an interpretation was compared with published well  
175 log data, seismic reflection profile and isobaths maps (Mazzoli et al., 2006, 2014; Nicolai and  
176 Gambini, 2007). The original jpeg images were first converted into seg-y files, by using the  
177 image2segy 2.2.6 Matlab script developed by the Instituto de Ciències del Mar (Barcelona,  
178 Spain), and then imported into the Move<sup>TM</sup> software for subsequent digitalization of the main  
179 stratigraphic horizons and fault surfaces. Afterwards, the time-to-depth conversion was  
180 computed by assigning a specific velocity value to the individual tectono-stratigraphic units  
181 (Dix, 1955; Improta et al., 2000). (insert Figure 3).

182

### 183 *3.3 3D geological reconstruction*

184 This work involved several steps of activities aimed at reconstructing both stratigraphic and  
185 tectonic surfaces pertaining to the Monte Alpi Unit. First, the Digital Elevation Model  
186 (DEM), the large-scale geological map, and all the available subsurface data in jpeg format  
187 were imported into Gocad®, and then georeferenced for calibration and consistency checking.  
188 The imported DEM was characterized by a 20x20 m resolution. A triangulated mesh was built  
189 from the DEM data points using both the Delaunay triangulation and interpolation in order to  
190 obtain a continuous and optimized representation of the topography (Mallet et al., 2002).  
191 Then, the georeferenced geological map was draped onto the topographic surface to obtain a  
192 textured topographic surface.

193 In order to constrain the buried portions of the Apulian carbonates, we performed time-to-  
194 depth conversion of four seismic profiles by using the GeolToolbox plugin ([www.ring-team.org/consortium](http://www.ring-team.org/consortium)). Furthermore, six geological cross-sections obtained from the published  
195 geological map of Monte Alpi (La Bruna et al., 2017) and existing bibliography related to  
196 geometry of the buried Top Apula surface underneath the southern Apennines FTB (Nicolai  
197 and Gambini, 2007) were taken into account. The eight stratigraphic logs performed in  
198

199 correspondence of the outcropping mixed carbonate-terrigenous Messinian cover were also  
200 imported in GOCAD. The 3D geological model of Monte Alpi was finally obtained by  
201 constructing the individual fault and stratigraphic surfaces by using the Discrete Smooth  
202 Interpolation tool (Mallet, 1989; Mallet et al., 2002), which allowed to constrain on fault-fault  
203 and fault-stratigraphic surfaces in the light of the aforementioned data. Both resolution and  
204 convergence criteria were defined according to the protocol recommended by Caumon et al.,  
205 (2009).

206

### 207 *3.4 Fault analysis*

208 Fault throw computation for individual faults was carried out by considering the cutoff lines  
209 along the fault hanging walls (Figure 4). This data was obtained by following the  
210 aforementioned procedure, in which the individual stratigraphic surfaces were cut by the  
211 high-angle fault surfaces. Subsequently, as a first step, the total amount of throw distribution  
212 (cumulative throw) was computed for each fault surface. This value corresponded to the  
213 current vertical offset of the bottom Early Cretaceous surface. Then, the pre-Messinian throw  
214 distribution was calculated by subtracting the amount of Early Messinian vertical  
215 displacement from the cumulative throw. Similarly, the Early Messinian throw data were  
216 obtained by subtracting the amount of Late Messinian vertical displacement from the pre-  
217 Messinian throw data. (insert Figure 4).

218

## 219 **4. Results**

### 220 *4.1 Syn-sedimentary extensional faulting*

#### 221 *1 - Mesozoic carbonates*

222 Mid-Upper Jurassic carbonates crop out only along the NW edge of Monte Alpi (Figure 5a),  
223 whereas the Lower Cretaceous ones are widespread in the study area (De Lorenzo, 1895;

224 Selli, 1957; Sartoni and Crescenti, 1962; Grandjacquet, 1963; Roda, 1965; Ogniben, 1969).  
225 The former carbonates consist of greyish-to- black limestones and minor dolomites, which are  
226 conformably overlain by Lower Cretaceous, peritidal, whitish-to-dark grey limestones  
227 showing multiple dissolution evidences such as karst solution grooves and fissures. Both  
228 Jurassic and Lower Cretaceous limestone beds are quite tabular, 10's of cm- to m-thick, and  
229 commonly consist of grainstones and packstones, and less frequent mudstones, wackestones,  
230 bindstones, floatstones and rudstones (Dunham, 1962; Embry and Klovan, 1971). Results of  
231 thin section analysis are consistent with abundance of benthic foraminifera, peloids, and  
232 fenestral structures within both Jurassic and Lower Cretaceous carbonate rocks (Figures 5b-f).  
233 In particular, the Jurassic limestones include cm-sized stromatoporoids (*Cladocoropsis*  
234 *mirabilis*, Figure 5b), whereas the Cretaceous ones contain oolites (Figure 5c) and red algae  
235 (*Salpingoporella annulata*, Figures 5d and f). Dolomites are petrographically heterogeneous  
236 in texture, crystal size, and crystal shape (Rustichelli, personal communication); late  
237 diagenetic fabric-destructive zebra (saddle) dolomites are also documented (Figure 5g).  
238 Blocky calcite cement fills the pore space. Calcite veins, rare quartz veins, and dark  
239 microstylolites crosscut the Mesozoic carbonates (La Bruna et al., 2017). Along the western  
240 cliff of the carbonate massif, within the Lower Cretaceous limestones, a ENE-striking, NNW-  
241 dipping, syn-sedimentary normal fault is documented (Figures 5a and h). There, the carbonate  
242 succession shows an increase of thickness toward the major slip surface (Figures 5h and i).  
243 (insert Figure 5).

#### 244 *II - Lower Messinian carbonates*

245 Up to 35 m-thick, Lower Messinian limestones crop out along both the western cliff of Monte  
246 Alpi and the eastern slope of the Santa Croce Peak (cf. Figures 2 and 6a). These limestones  
247 consist mainly of grey-to-dark gray skeletal grainstones with minor packstones, floatstones,  
248 rudstones and bindstones (Figures 6b-g). Biota is dominated by red algal (*Lithothamnium*)

249 debris with minor benthic foraminifera, echinoid plates and spines, and fragments of serpulids  
250 (*Ditrupa*) and bivalves, collectively pointing to an inner-middle ramp depositional setting.  
251 The individual limestone beds are tabular, laterally continuous, characterized by a thickness  
252 variation comprised between 10's of cm and ca. 4 m, and show thinning upward trends. The  
253 topmost portion of the Lower Messinian limestones is made up of thinly-bedded, bituminous,  
254 planktonic foraminiferal wackestones including fish remains and intervening marl beds  
255 (Figures 6b-f). The Lower Messinian limestones, which include blocky calcite cements, dark  
256 stylolites, and multiple sets of calcite veins, were originally deposited in an outer ramp  
257 depositional setting, which became progressively deeper with time (Taddei and Siano, 1992;  
258 La Bruna et al., 2017). ENE-striking, and both NNW- and SSE-dipping, syn-sedimentary  
259 normal faults are exposed along the north-eastern sector of Monte Alpi (Figures 6a and h).  
260 These faults produced an accommodation space in their hanging wall in which limestone beds  
261 were deposited (Figures 6h and i). The two sets of ENE-striking faults form a conjugate fault  
262 system that also crosscut the Lower Cretaceous limestone rocks, causing roll over (higher dip  
263 angles towards the faults) of the limestone beds located at the hanging wall of the major,  
264 Early Messinian normal fault. (insert Figure 6).

### 265 *III - Upper Messinian terrigenous deposits*

266 The Upper Messinian siliciclastic beds, which respectively form both onlap and downlap  
267 geometries with the high-angle faults and low-angle erosional surfaces crosscutting both  
268 Lower Cretaceous and Lower Messinian limestones (Figures 7a and b), are made up of  
269 conglomerates, sandstones and siltstones. The heterometric conglomerates include sub-  
270 rounded to flattened, polygenic pebbles (Figure 7c), whereas the litharenitic sandstones  
271 contain coarse-to-thin rock fragments arranged in either parallel or cross laminated beds  
272 (Figure 7d). The former rocks are located at the western and north-eastern edges of Monte  
273 Alpi, whereas the sandstones throughout its north-eastern and eastern sectors (La Bruna et al.,

274 2017). The exposed Upper Messinian succession is up to ca. 300 m-thick. (insert Figure 7).  
275 To better decipher its depositional architecture, multiple stratigraphic logs have been  
276 measured throughout the study area. Logs #1 to #4 highlight the northward thinning of  
277 conglomerates along the southern sector of Monte Alpi, whereas logs #5 to #7 show their  
278 westward thinning along its eastern sector (Figure 8). (insert Figure 8).  
279 By considering thickness variations of the Upper Messinian terrigenous deposits, an isopach  
280 map of the Upper Messinian deposit is computed, which shows that the two maxima located  
281 at the SW and NW edges of Monte Alpi are bound by the F2 and F3 Faults (Figure 9a). A  
282 third, less pronounced maximum is also computed at the intersection of the two  
283 aforementioned faults. In order to decipher the bedding attitude of both Lower Cretaceous and  
284 Lower Messinian limestones at the onset of deposition during Upper Messinian, data are  
285 restored accordingly (Figure 9b). Results are consistent with the west- and southwest-dipping  
286 limestone beds of the Canale del Grillone area, western sector of Monte Alpi, separated by a  
287 structural horst bounded by both F4 and F5 Faults from northeast-dipping beds of the Santa  
288 Croce area, eastern sector of Monte Alpi. (insert Figure 9).

289

#### 290 *4.2 Fault dimensional analysis*

291 The 3D geological model constructed for the whole study area consists of a  $2 \cdot 10^3 \text{ km}^3$   
292 volume that includes three stratigraphic surfaces pertaining to the Monte Alpi Unit, and forty-  
293 three fault surfaces. Both dip azimuth and dip angle data were then computed for the largest,  
294 twenty-seven fault surfaces (Figure 10a, Table1). Results are shown with histograms (Figures  
295 10b and 10c). (insert Figure 10 and Table 1). According to their strike direction, the twenty-  
296 seven fault surfaces are sorted into the following five sets:

297 Set 1 - NW-SE faults with throws between 100 and 1,300 m;

298 Set 2 - NNW-SSE faults with throws between 100 and 1,300 m;

299 Set 3 - ENE-WSW faults with throws between 50 and 800 m;

300 Set 4 - WNW-ESE faults with throws between 170 and 1,100 m;

301 Set 5 - NNE-SSW faults with throws between 50 and 150 m.

302 Results of mesoscale structural analysis performed at specific outcrops have been used to  
303 better constrain both attitude and kinematics of individual fault sets, as well as to document  
304 their relative abutting and crosscutting relationships (Figure 11). Sets 1 and 2 mainly consist  
305 of left-lateral, strike-slip faults, which were then re-activated as normal faults during the latest  
306 exhumation stages (La Bruna et al., 2017). Sets 3 and 4 comprise normal faults likely re-  
307 activated as reverse faults during Early Pleistocene times (Van Dijk et al., 2000), whereas Set  
308 5 only includes normal faults. (insert Figure 11).

309

#### 310 *4.3 Fault throw analysis*

311 Fault throw analysis is carried out by taking the computed cumulative throw ( $D$ ) and length  
312 ( $L$ ) values into account. Error bars were estimated for the individual fault surfaces (cf. Figure  
313 4) on the basis of the resolution obtained. Errors are reported hereafter.  $D$ :  $\pm 50\text{m}$  (F1, F2, F3  
314 and F5 Faults),  $\pm 10\text{m}$  (F4 Fault),  $\pm 5\text{m}$  (F6, F7, F9 and F12 Faults),  $\pm 2\text{m}$  (F8 Fault),  $\pm 1\text{m}$   
315 (F11 Fault), and  $\pm 0,5\text{m}$  (F10 Fault).  $L$ :  $\pm 50\text{m}$  (F1, F2, F3, F5, F11 and F12 Faults),  $\pm 25\text{m}$   
316 (F4, F6, F7, F8, F9 and F10 Faults).

317 Results of throw-length computations are consistent with different shapes of the fault throw  
318 profiles (Fig. 12). In fact, both F10 and F3 faults show symmetric, bell-shaped profiles,  
319 whereas F6, F8, and F12 faults are characterized by flat-topped profiles. Moreover, F1, F4,  
320 and F11 faults show asymmetric profiles with steep gradients towards one of the fault tips,  
321 whereas F2, F5, F7, and F9 faults display asymmetric profiles with steep gradients toward  
322 both fault tips. (insert Figure 12).

323 The computed pre-Messinian, Early Messinian, and post-Early Messinian throw profiles are  
324 reported in Figure 13, and summarized in the following text (negative values correspond to  
325 either reverse displacements or rotated normal faults). (insert Figure 13).

326 F1 Fault (Set 2): the post-Early Messinian throw profile shows an asymmetric shape, with  
327 values increasing towards the NNW edge; along the central portion of the fault, the profile is  
328 flat-topped. The Early Messinian throw profile does not record any displacement, whereas the  
329 pre-Messinian throw profile shows two maxima separated by a flat-topped throw profile.

330 F2 Fault (Set 1): the post-Early Messinian throw profile shows a bell-shaped geometry, with a  
331 very pronounced peak in the central portion of the fault. The Early Messinian throw profile  
332 does not show any displacement, whereas pre-Messinian throw profile displays both a flat-  
333 topped geometry at ca. -200 m-throw along the NW edge, and a bell-shaped geometry, with a  
334 peak at ca. 450 m-throw, along the SE edge.

335 F3 Fault (Set 3): the post-Early Messinian throw profile shows a bell-shaped geometry, with  
336 two nearby maxima in the central portion of the fault. The Early Messinian throw profile  
337 shows a slightly asymmetric geometry, with higher values towards the WSW edge of the  
338 fault. The pre-Messinian throw profile displays a flat-topped geometry at around 100 m-  
339 throw.

340 F4 Fault (Set 1): the post-Early Messinian throw profile shows an asymmetric shape, with the  
341 greater values towards the NW edge of the fault. The Early Messinian throw profile does not  
342 show any displacement, whereas the bottom pre-Messinian throw profile displays a slightly  
343 pronounced, bell-shaped geometry towards the NW edge of the fault.

344 F5 Fault (Set 1): the post-Early Messinian throw profile shows a sort of asymmetric  
345 geometry, with the greatest values localized at the NW edge of the fault. The Early Messinian  
346 throw profile shows a flat-topped geometry, with values at ca. 100 m-throw. The pre-

347 Messinian throw profile displays two flat-topped geometries, localized at values of ca. 100 m.  
348 and -100 m-throw, respectively.

349 F6 Fault (Set 3): the post-Early Messinian throw profile forms a smooth, flat-topped  
350 geometry. Both Early Messinian and pre-Messinian throw profiles do not show any  
351 significant displacement.

352 F7 Fault (Set 3): the post-Early Messinian throw profile displays an asymmetric shape, with a  
353 maximum towards the WSW edge of the fault. The Early Messinian throw profile does not  
354 show any displacement, whereas the bottom pre-Messinian throw profile displays an  
355 asymmetric geometry characterized by two maxima localized at the fault tips.

356 F8 Fault (Set 3): the post-Early Messinian throw profile shows an asymmetric shape, with the  
357 greatest displacement localized at the WSW edge of the fault. The Early Messinian throw  
358 profile displays a very small amount of displacement, with a flat-topped geometry at ca. 70  
359 m-throw. The pre-Messinian throw profile shows an asymmetric shape, with the greatest  
360 negative values towards the WSW edge of the fault.

361 F9 Fault (Set 1): the post-Early Messinian throw profile shows a bell-shaped geometry, with a  
362 maxima at around 100 m-throw. The Early Messinian throw profile shows a flat-topped  
363 geometry at around 60 m-throw. The pre-Messinian throw profile shows an asymmetric  
364 shape, with a maximum towards the SE edge of the fault.

365 F10 Fault (Set 4): all stratigraphic horizons display a flat-topped geometry, with a maximum  
366 of ca. 50 m-throw.

367 F11 Fault (Set 2): all stratigraphic horizons display a flat-topped geometry, with a maximum  
368 of ca. 90 m-throw (post-Early Messinian) and 50 m-throw (pre-Messinian and Early  
369 Messinian), respectively.

370 F12 Fault (Set 3): the post-Early Messinian throw profile shows a bell-shaped geometry, with  
371 a maximum at ca. 200 m-throw. The Early Messinian profile shows a flat-topped geometry

372 localized in the WSW portion of the fault at ca. 80 m-throw. The pre-Messinian profile  
373 displays a bell-shaped geometry, with negative values down to around -120 m-throw.

374

#### 375 *4.4 Fault scaling properties*

376 Based upon the fault throw profiles shown above, the maximum computed vertical  
377 Displacement (D) - Length (L) data for the twelve faults (Table 2) that dissect the exposed  
378 Monte Alpi Unit are plotted in a log-log diagram (Figure 14a). As reported in the first section  
379 of the manuscript, the slope of the computed power law, best-fit line corresponds to the  
380 growth line of individual, isolated faults (Cartwright et al., 1995). As a result, a  $n$  value of ca.  
381 1 is computed for the pre-Messinian faults. We note that a  $n$  value of ca. 0.8 is computed for  
382 the three faults active during Lower Messinian (Figure 14b), which is obviously not  
383 statistically significant due to the small number of data points (Massot et al., 2002).  
384 Differently, a  $n$  value of ca. 1.5 was computed for the post-Early Messinian fault growth line  
385 (Figure 14c). (insert Table 2 and Figure 14).

386

## 387 **5. Data interpretation and discussion**

### 388 *5.1 Fault growth mechanisms*

389 The most pronounced strike variations are computed for Set 1 Faults (Table 1). Assuming that  
390 these faults developed by mean of subsidiary, extensional faults localized at their releasing  
391 jogs and/or at the extensional quadrants of mode-II edges (Segall and Pollard, 1980, 1983;  
392 Mollema and Antonellini, 1999; Myers and Aydin, 2004; Flodin and Aydin, 2004; Agosta  
393 and Aydin, 2006; Antonellini et al., 2008; Agosta et al., 2010; Aydin et al., 2010), these  
394 variations could be due to either Early Pleistocene or Middle Pleistocene strike-slip tectonics.  
395 In fact, many authors assessed the occurrence of strike-slip along NW-SE striking faults  
396 exposed in the study area, and its surrounding regions, during Quaternary times (Knott 1987;

397 Carbone et al., 1991; Monaco and Tansi, 1992; Oldow et al., 1993; Monaco and Tortorici,  
398 1998; Cello and Mazzoli, 1998; Tavarnelli and Pasqui, 2000; Van Dijk et al., 2000; Lentini et  
399 al., 2002; Mazzoli et al., 2006, 2014; La Bruna et al., 2017). Bearing the aforementioned  
400 interpretation in mind, the modalities of growth of the Monte Alpi extensional fault network  
401 are discussed hereafter by considering the computed fault throw profiles. Bell-shaped, flat-  
402 topped, and asymmetric cumulative fault throw profiles (Figure 12) indicate presence of  
403 isolated fault segments that likely interacted with each other during deformation (Muraoka  
404 and Kamata, 1983; Barnet et al., 1987; Walsh and Watterson, 1987, 1988, 1990; Peacock and  
405 Sanderson, 1991; Cowie and Scholz, 1992a; Cartwright et al., 1995; Huggings et al., 1995;  
406 Nicol et al., 1996; McLeod et al., 2000; Manighetti et al., 2001; Schlagenhauf et al., 2008).

407 A more detailed interpretation of the growth mechanisms can be deciphered by considering  
408 the pre-Messinian, Early Messinian, and post-Early Messinian fault throw profiles (Figure  
409 13), and the results of stratigraphic field logging (Figure 8), Upper Messinian isopach map  
410 computation (Figure 9), and detailed field structural analyses (Figures 5 to 7). The pre-  
411 Messinian fault network was comprised of Sets 1, 2, and 3 faults, respectively striking NW-  
412 SE, NNW-SSE, and ENE-WSW. Among all the inferred syn-sedimentary Early Cretaceous  
413 faults, the greatest throw values were computed for Set 1 faults. The computed throw data for  
414 Sets 1 and 2 faults show that they were likely comprised of original, isolated fault segments,  
415 up to a few km-long, and characterized by bell-shaped throw profiles. The computed  $n$  value,  
416 ca. 1, indicates that these faults grew under constant driving stress conditions (Schultz et al.,  
417 2008), forming self-similar geometries (Mandelbrodt and Pignoni, 1983; Torabi and Berg,  
418 2011). However, interaction and possible linkage processes (Walsh and Watterson, 1988)  
419 occurred among the isolated fault segments, as suggested by the wide data point dispersion  
420 (Figure 14a). Such a dispersion shifted the power law best fit line with respect to the  
421 theoretical fault growth line, traced according to the highest displacements values (Schultz et

422 al., 2010). Linkage processes took place in correspondence of stepover/relay zones (Trudgill  
423 and Cartwright, 1994; Fossen and Rotevatn, 2016), and determined lower D/L values for  
424 given fault lengths (Figure 14d). Then, displacement localization within the linkage zones due  
425 to enhanced shear stress (Aydin and Schultz, 1990) caused higher D/L values up to the  
426 theoretical fault growth line (Cowie and Scholz, 1992a,b; Cartwright et al., 1995; Mansfield  
427 and Cartwright, 1996).

428 Regarding the age of faulting, Sets 1 and 2 faults are ca. sub-parallel to those crosscutting the  
429 Outer Apulian Platform, and exposed at the Gargano Promontory and Murge Plateau of  
430 southern Italy (cf. inset of Figure 1). Since the latter faults were interpreted as Cretaceous  
431 structures (Bertotti, 2001; Korneva et al., 2014; Laurita et al., 2016; Petruccio et al., 2017;  
432 Vitale et al., 2017), a similar age is hence proposed for the study faults. In fact, these Sets 1  
433 and 2 faults were likely coeval to the Set 3 faults, which strike ENE-WSW, documented along  
434 the western cliff of the Monte Alpi (Figures 5a and 5h).

435 The pre-Messinian, likely Early Cretaceous in age, fault system was re-activated during onset  
436 of the Monte Alpi foreland basin system, as suggested by both computed (Figure 13) and  
437 measured structural data (Figures 6a, h, i). This fault system included either isolated (*ie.* F5  
438 and F12 faults), or interacting faults (*ie.* F3 Fault), which were characterized by flat-topped  
439 and asymmetric profiles, respectively. Focusing on post-Early Messinian times, all faults  
440 pertaining to the Monte Alpi network show evidences of slip. The computed  $n$  value is about  
441 1.5 (Figure 14c). This value, which is significantly greater than those computed for both pre-  
442 Messinian and Early Messinian faults, is therefore consistent with a scale-dependent geometry  
443 of the post-early Messinian fault network (Watterson, 1986; Walsh and Watterson, 1988;  
444 Cowie and Scholz, 1992a,b; Scholz et al., 1993; Schlische et al., 1996; Kim and Sanderson,  
445 2005; Schultz et al., 2008).

446 By considering both T- and Y-shaped intersections, we observe that the former geometry is

447 quite common in the modelled fault system (Figures 10, 14e). In fact, these types of  
448 intersection characterize F6, F7 and F8 faults, which are bounded on both sides by the F4 and  
449 F5 and the F5 and F8 faults, respectively. On the other hand, the bounding F4 and F5 faults  
450 intersect southward the F3 fault also forming T-shaped intersections. Among these, we focus  
451 on the detailed throw profile analysis of both F7 and F5 faults (Figure 14e), which dropdown  
452 the same block but unfortunately do not show very significant evidences of mechanical  
453 interaction (Walsh et al., 2003). Differently, the T-shaped intersection formed by both F5 and  
454 F3 faults is characterized by a marked increases of vertical displacement in the zone where  
455 the two fault footwalls coincide (Fig. 14e). Y-shaped intersections are investigated by  
456 considering small (ca.  $30^\circ$ ) and large (ca.  $130^\circ$ ) alpha angles (Maerten et al., 1999). The  
457 former case is displayed by the F11 Fault intersecting against the F4 Fault (Fig 14e). There, a  
458 pronounced increase of vertical displacement occurs in the zone where the two fault footwalls  
459 coincide (Fig. 13). The latter case if formed by the F12 Fault intersecting the F5 Fault (Fig.  
460 14e), but the two fault throw profiles do not show any variation in coincidence of the  
461 intersection line (Fig. 13).

462

### 463 *5.2 Implication for the evolution of the Messinian foreland basin system*

464 Results of the integrated field and laboratory analyses are consistent with a pre-Messinian  
465 orthogonal fault system made up of isolated, interacting faults (Figure 15). During Early  
466 Messinian times, with ongoing roll-back of the Apulian Platform (Royden et al., 1993;  
467 Doglioni, 1999), shallow-water marine basins characterized by anoxic conditions (Taddei and  
468 Siano, 1992) formed within the back-bulge deposition zone of the Inner Apulian Platform  
469 (Patacca et al., 1992; Critelli et al., 2011; Vitale et al., 2012) or, alternatively, within outer  
470 secondary basins (sensu Flemings and Jordan, 1989). According to both basin geometry and  
471 infill, similar conclusions were proposed for the Sunda shelf region, Indonesia (Ben Avraham

472 and Emery, 1973), the Cordilleran foreland basin, USA (DeCelles and Burden, 1992; Plint et  
473 al., 1993) and the Taranaki foreland basin, New Zealand (Holt and Stern, 1994). The Early  
474 Messinian basin of Monte Alpi was mainly bounded by re-activated Set 1 (NW-SE) and Set 3  
475 (ENE-WSW) faults. Activity of an orthogonal fault system during the earliest stages foreland  
476 basin systems evolution was already documented by Tavani et al. (2015b) in the Prenestini  
477 Mt. of central Apennines, Italy, and interpreted as due to along-foredeep stretching (Tavani et  
478 al., 2015a). This process commonly takes place in correspondence of curved orogens  
479 (Doglioni, 1995; Zhao and Jacobi, 1997; Whitaker and Engelder, 2006), such as the southern  
480 Apennines FTB (Locardi, 1988).

481 Differently, the erosional surface topping the Early Messinian limestones possibly formed in  
482 the forebulge (Figure 15), which is an area commonly characterized by a significant uplift  
483 (DeCelles and Giles, 1996), and considered as a non-depositional and/or erosional zone  
484 (Flemings and Jordan, 1989; Crampton and Allen, 1995). On the basis of the restored bottom  
485 Late Messinian surface (Figure 6l), a structural horst bounded by Set 1 faults formed at that  
486 time. This deformation caused emersion, and partial erosion, of both Mesozoic and Lower  
487 Messinian carbonates. Subsequently, the stratigraphy of the Late Messinian deposit also  
488 suggests that nucleation of the Monte Alpi foredeep basin was controlled by re-activation of  
489 Set 3 faults (ENE-WSW), whereas as shown by the computed fault throw profiles its later  
490 development was mainly due to activity of Set1 fault (NW-SE).

491 According to Walsh et al. (2002), we interpret that the steeper slope of the post-Early  
492 Messinian fault growth line with respect to both pre-Messinian and Early Messinian lines  
493 (Figures 14a to c) reflects the higher degree of maturity of the post-Early Messinian fault  
494 network (Cartwright et al., 1995; Nicol et al., 1996; Gupta and Scholz, 2000), and/or the  
495 pronounced lithostatic loading that occurred during post-Messinian times (Mazzoli et al.,  
496 2006). Focusing on Late Messinian times, the foredeep basin was characterized by isolated

497 depocenters, in which up to 600 m-thick terrigenous sediments were deposited (Monaco et al.,  
498 1998; cf. well 2 of Figure 2). Compared to the 1,000's m-thick Lower Pliocene (Casero, 2004;  
499 Shiner et al., 2004) and Upper Pliocene-Lower Pleistocene foredeep infills (Balduzzi et al.,  
500 1982, Casnedi, 1988a, b), the Late Messinian succession is interpreted as due to a first-order  
501 stage of forebulge progradation (Catuneanu, 2004), which occurred during thrusting of the  
502 outermost portions of the southern Apennines FTB (Marabini and Vai, 1985; Cavazza and  
503 DeCelles, 1998; Vitale and Ciarcia, 2013). It can be therefore argued that the Messinian  
504 foreland basin system of Monte Alpi developed during a rapid migration of the southern  
505 Apennines FTB, which triggered a predominant elastic response to flexure of the Apulian  
506 plate due to the low amount of its tectonic load (Crampton and Allen, 1995; DeCelles and  
507 Giles, 1996; Catuneanu, 2004). (insert Figure 15).

508

## 509 **6. Conclusions**

510 The present work combined geological field mapping and stratigraphic logging with  
511 subsurface seismic and well log data interpretation to perform the 3D geological  
512 reconstruction of the Monte Alpi area, southern Italy. The goals were the assessment of both  
513 growth mechanisms and scaling properties of the pre-Pliocene fault network, and the  
514 understanding of the structural control played by high-angle extensional faults on the time-  
515 space evolution of the Messinian foreland basin system. Field analyses were aimed at  
516 assessing the stratigraphy of the Messinian mixed carbonate-terrigenous deposits, and at  
517 documenting Early Cretaceous, Early Messinian, and Late Messinian syn-sedimentary faults.  
518 Seismic reflection profiles and well logs were interpreted in order to decipher the geometry of  
519 the topmost surface of the Monte Alpi Unit. Results of both surface and subsurface analyses  
520 were then input in Gocad® to perform the 3D geological reconstruction of the Monte Alpi  
521 massif and its surrounding areas. This procedure was then followed by the computation of

522 Late Messinian isopach map, and of throw profiles for the individual structures forming the  
523 Monte Alpi fault network. Results after 3D geological modelling and throw profile analysis  
524 were discussed to assess its following time-dependent evolution:

- 525 • During pre-Messinian times, main NW-SE to NNW-SSE fault segments were active  
526 as isolated structures, which likely interacted and linked together during ongoing  
527 deformation. According to literature data, these faults likely formed during Early  
528 Cretaceous times within the Inner Apulian Platform. Field evidences also show minor  
529 ENE-WSW, Early Cretaceous, syn-sedimentary extensional faults. Dimensional  
530 properties computed for the NW-SE to NNW-SSE faults showed that these features  
531 formed as isolated faults within a network characterized by self-similar geometries.
- 532 • During Early Messinian time, most of the pre-existing NW-SE and ENE-WSW faults  
533 were re-activated in the back-bulge zone during the earliest stages of foreland basin  
534 system evolution. These faults bounded shallow-water marine basins, in which  
535 carbonate sediments were deposited under anoxic conditions. The computed  
536 dimensional properties are also consistent with a self-similar fault network.
- 537 • Subsequently, isolated structural horsts formed in the forebulge zone of the foreland  
538 basin system. The horsts were bounded by NW-SE faults, which caused uplift, tilting,  
539 and partial erosion of both Mesozoic and Lower Messinian carbonates.
- 540 • During Late Messinian times, a 100's m-deep foredeep basin characterized by half-  
541 graben depocenters bounded by NW-SE faults developed in the study area. Minor  
542 ENE-WSW faults were likely active during that time, forming a scale-dependent  
543 network in which the individual faults intersected the previously formed structures  
544 producing higher displacement/length values.

545 The complex tectonic evolution that affected the study area since Early Pliocene times  
546 profoundly modified the aforementioned structural configuration, and partially obliterated

547 the original fault network. However, the results presented in this work shed a new light  
548 into the structural control exerted by inherited faults on the development of the Messinian  
549 foreland basin system of Monte Alpi. Further analysis focused on the sedimentological  
550 and petrographic characterization of the Messinian mixed carbonate-terrigenous deposits  
551 are required to better assess the geometry of the depositional environments, and their  
552 relationships with the bounding high-angle faults.

553

#### 554 **Acknowledgments**

555 The present work is part of the first author's Ph.D. Thesis Dissertation. Authors want to thank  
556 Enrico Tavernelli and an anonymous reviewer for their advices and their helpful correction on  
557 the paper manuscript. VLB acknowledges Stefano Mazzoli, Italo Sgrosso, Marcello  
558 Schiattarella, Jean Borgomano, Sergio Longhitano and Carlos Pirmez for their thoughtful and  
559 constructive discussions. The first author also acknowledges the great support provided by  
560 Paola Castelluccio, Alessandro Giuffrida, Arturo La Bruna, Andrea Rustichelli, Anthony  
561 Tendill, Christophe Matonti, and Sebastien Chatelée during field and laboratory analyses.  
562 This work was supported by the Ministry of Education, University and Research (MIUR), and  
563 by the Reservoir Characterization Project, a consortium of universities and energy companies  
564 ([www.rechproject.com](http://www.rechproject.com)). ENI is acknowledged for providing seismic reflection data pertaining  
565 to the Monte Alpi and surrounding areas.

566

567

568 **References**

- 569 Agosta, F., Aydin, A., 2006. Architecture and deformation mechanism of a basin-bounding  
570 normal fault in Mesozoic platform carbonates, central Italy. *Journal of Structural*  
571 *Geology* 28, 1445-1467.
- 572 Agosta, F., Alessandroni, M., Tondi, E., Aydin A., 2010. Oblique normal faulting along the  
573 northern edge of the Majella anticline, central Italy: Inferences on hydrocarbon migration  
574 and accumulation. *Journal of Structural Geology* 32, 1317-1333.
- 575 Alberti, M., Lapenta, M.C., Maurella, A., 2001. New geological data on the basin units  
576 surrounding the Monte Alpi unit (southern Italy). *Bollettino della Società dei Naturalisti in*  
577 *Napoli - Nuova Serie*, 1, 85-96.
- 578 Antonellini, M., Tondi, E., Agosta, F., Aydin, A., Cello G., 2008. Failure modes in deep-  
579 water carbonates and their impact for fault development: Majella Mountain, Central  
580 Apennines, Italy. *Marine and Petroleum Geology* 25, 1074-1096.
- 581 Aydin, A., Schultz, R. A., 1990. Effect of mechanical interaction on the development of  
582 strike-slip faults with echelon patterns. *Journal of Structural Geology* 12, 123-129.
- 583 Aydin, A., Antonellini, M., Tondi, E., Agosta F., 2010. Deformation along the leading edge  
584 of the Maiella thrust sheet in central Italy. *Journal of Structural Geology* 32, 1291-1304.
- 585 Balduzzi, A., Casnedi, R., Crescenti, U., Mostardini, F., Tonna, M., 1982. Il Plio-Pleistocene  
586 del sottosuolo del bacino lucano (Avanfossa appenninica). *Geologica Romana* 21, 1-28.
- 587 Barnett, J. A., Mortiner, J., Rippon, J. H., Walsh, J. J., Waternson, J., 1987. Displacement  
588 geometry in the volume containing a single normal fault. *AAPG Bulletin* 71, 925-937.
- 589 Ben-Avraham, Z., Emery, K. O., 1973. Structural framework of Sunda shelf. *AAPG Bulletin*  
590 57, 2323-2366.

- 591 Bertok, C., Martire, L., Perotti, E., d'Atri, A., Piana, F., 2012. Kilometre-scale  
592 palaeoscarpements as evidence for Cretaceous synsedimentary tectonics in the external  
593 Briançonnais domain (Ligurian Alps, Italy). *Sedimentary Geology* 251-252, 58-75.
- 594 Bertotti, G., Picotti, V., Chilovi, C., Fantoni, R., Merlini, S., Mosconi, A. 2001. Neogene to  
595 Quaternary sedimentary basins in the south Adriatic (Central Mediterranean): foredeeps  
596 and lithospheric buckling. *Tectonics* 20, 771-787.
- 597 Boccaletti, M., Ciaranfi, N., Cosentino, D., Deiana, G., Gelati, R., Lentini, F., Tortorici, L.,  
598 1990. Palinspastic restoration and paleogeographic reconstruction of the peri-Tyrrhenian  
599 area during the Neogene. *Palaeogeography, Palaeoclimatology, Palaeoecology* 77, 41-50.
- 600 Bonardi, G., Ciarcia, S., Di Nocera, S., Matano, F., Sgrosso, I., Torre, M., 2009. Carta delle  
601 principali unità cinematiche dell'Appennino meridionale. Nota illustrativa. *Bollettino della*  
602 *Società Geologica Italiana* 128, 47-60.
- 603 Borgomano, J. R. F., 2000. The Upper Cretaceous carbonates of the Gargano-Murge region,  
604 southern Italy: a model of platform-to-basin transition. *AAPG bulletin* 84, 1561-1588.
- 605 Butler, R.W.H., Mazzoli, S., Corrado, S., De Donatis, M., Scrocca, D., Di Bucci, D.,  
606 Gambini, R., Naso, G., Nicolai, C., Shiner, P., Zucconi, V., 2004. Applying thick-skinned  
607 tectonic models to the Apennine thrust belt of Italy – Limitations and implications. In:  
608 *Thrust tectonics and hydrocarbon systems* (K.R. McClay, ed.). *American Association of*  
609 *Petroleum Geologists* 82, 647-667.
- 610 Carbone, S., Catalano, S., Lentini, F., Monaco, C., 1988. Le unità stratigrafico-strutturali  
611 dell'Alta Val d'Agri (Appennino lucano) nel quadro dell'evoluzione del sistema catena-  
612 avanfossa. *Memorie Società Geologica Italiana* 41, 331-341.
- 613 Carbone, S., Lentini, F., 1990. Migrazione neogenica del sistema catena-avampaese  
614 nell'Appennino meridionale: problematiche paleogeografiche e strutturali. *Rivista Italiana*  
615 *di Paleontologia e Stratigrafia* 96, 271-296.

- 616 Carbone, S., Catalano, S., Lentini, F., Monaco, C., 1991. Carta geologica del bacino del fiume  
617 Agri. Scala 1:50.000. Cartografia SELCA, Firenze.
- 618 Cartwright, J., Trudgill, B. D., Mansfield, C. S., 1995. Fault growth by segment linkage: an  
619 explanation for scatter in maximum displacement and trace length data from Canyonlands  
620 Graben of SE Utah. *Journal of Structural Geology* 17, 1319-1326.
- 621 Casero, P., 2004. Structural setting of petroleum exploration plays in Italy. Special volume of  
622 the Italian Geological Society for the IGC 32, 189-199.
- 623 Casnedi, R., 1988a. La Fossa bradanica: origine, sedimentazione e migrazione. *Memorie*  
624 *Società Geologica Italiana* 41, 439-448.
- 625 Casnedi, R., 1988b. Subsurface basin analysis of fault-controlled turbidite system in Bradano  
626 trough, Southern Adriatic foredeep, Italy. *AAPG Bulletin* 72, 1370-1380.
- 627 Catalano, S., Monaco, C., Tortorici, L., Tansi, C., 1993. Pleistocene strike-slip tectonics in the  
628 Lucanian Apennine (Southern Italy). *Tectonics* 12, 656-665.
- 629 Catuneanu, O., 2004. Retroarc foreland systems evolution through time. *Journal of African*  
630 *Earth Sciences* 38, 225-242.
- 631 Caumon, G., Collon-Drouaillet, P., De Veslud, C. L. C., Viseur, S., Sausse, J., 2009. Surface-  
632 based 3D modeling of geological structures. *Mathematical Geosciences* 41, 927-945.
- 633 Cavalcante, F., Belviso, C., Finizio, F., Lettino, A., Fiore, S., 2009. Carta geologica delle  
634 Unità Liguridi dell'area del Pollino (Basilicata): Nuovi dati geologici, mineralogici e  
635 petrografici. Digilabs, Bari, 36.
- 636 Cavazza, W., DeCelles, P. G., 1998. Upper Messinian siliciclastic rocks in southeastern  
637 Calabria (southern Italy): palaeotectonic and eustatic implications for the evolution of the  
638 central Mediterranean region. *Tectonophysics* 298, 223-241.
- 639 Cavazza, W., Roure, F., Ziegler, P., 2004. The Mediterranean Area and the Surrounding  
640 Regions: Active Processes, Remnants of Former Tethyan Oceans and Related Thrust Belts.

- 641 In: W. Cavazza, F. Roure, W. Spakman, G.M. Stampfli and P Ziegler (Eds). The  
642 TRANSMED Atlas, 1-29.
- 643 Cello, G., Mazzoli, S., 1998. Apennine tectonics in southern Italy: a review. *Journal of*  
644 *Geodynamics* 27, 191-211.
- 645 Cowie, P. A., Scholz, C. H., 1992a. Physical explanation for the displacement-length  
646 relationship for faults using a post-yield fracture mechanics model. *Journal of Structural*  
647 *Geology* 14, 1133-1148.
- 648 Cowie, P. A., Scholz, C. H., 1992b. Displacement-length scaling relationships for fault: data  
649 synthesis and discussion. *Journal of Structural Geology* 14, 1149-1156.
- 650 Cowie, P. A., Roberts, G. P., 2001. Constraining slip rates and spacings for active normal  
651 faults. *Journal of Structural Geology* 23, 1901-1915.
- 652 Crampton, S. L., Allen, P. A., 1995. Recognition of forebulge unconformities associated with  
653 early stage foreland basin development: example from the North Alpine Foreland Basin.  
654 *AAPG bulletin* 79, 1495-1514.
- 655 Crider, J. G., Pollard, D. D., 1998. Fault linkage: Three-dimensional mechanical interaction  
656 between echelon normal faults. *Journal of Geophysical Research: Solid Earth* 103, 24373-  
657 24391.
- 658 Critelli, S., Muto, F., Perri, F., Tripodi, V., 2011. Relationships between lithospheric flexure,  
659 thrust tectonics and stratigraphic sequences in foreland setting: the southern Apennines  
660 foreland basin system, Italy. *InTech Open Access Publisher* 121-170.
- 661 D'Argenio, B., Pescatore, T., 1972. Schema geologico dell'Appennino Meridionale  
662 (Campania e Lucania). *Atti del Conv. Moderne vedute sulla geologia dell'Appennino*  
663 (Roma 16-18 Febbraio 1972). *Accademia Nazionale dei Lincei* 183, 49-72.
- 664 Dawers, N. H., Anders, M. H., 1995. Displacement-length scaling and fault linkage. *Journal*  
665 *of Structural Geology* 17, 607611-609614.

- 666 De Lorenzo, G., 1895. Osservazioni geologiche nell'Appennino della Basilicata meridionale.  
667 Atti Accademia di Scienza Fisica. Materiali 27, 31.
- 668 Destro, N., 1995. Release fault: A variety of cross fault in linked extensional fault systems, in  
669 the Sergipe-Alagoas Basin, NE Brazil. *Journal of Structural Geology* 17 615-629.
- 670 DeCelles, P. G., Burden, E. T., 1992. Non-marine sedimentation in the overfilled part of the  
671 Jurassic-Cretaceous Cordilleran foreland basin: Morrison and Cloverly Formations, central  
672 Wyoming, USA. *Basin Research* 4, 291-313.
- 673 DeCelles, P. G., Giles, K. A., 1996. Foreland basin systems. *Basin research* 8, 105-123.
- 674 Dewey, J. F., Helman, M. L., Turco, E., Hutton, D. H. W., Knott, S. D., 1989. Kinematics of  
675 the western Mediterranean. In Coward M. P., Dietrich D., Park R. G., eds., *Alpine*  
676 *Tectonics*. Geological Society of London Special Publication 45, 265-283.
- 677 Dix, C. H., 1955. Seismic velocities from surface measurements. *Geophysics* 20, 68-86.
- 678 Doglioni, C., 1991. A proposal for kinematic modeling of W-dipping subductions - Possible  
679 applications to the Tyrrhenian-Appennines system. *Terra Nova* 3, 423-434.
- 680 Doglioni, C., 1995. Geological remarks on the relationships between extension and  
681 convergent geodynamic settings. *Tectonophysics* 252, 253-267.
- 682 Doglioni, C., Gueguen, E., Harabaglia, P., Mongelli, F., 1999. On the origin of west-directed  
683 subduction zones and applications to the western Mediterranean. Geological Society,  
684 London, Special Publications 156, 541-561.
- 685 Dunham, R., 1962. Classification of Carbonate Rocks According to Depositional Textures. In  
686 W.E. Ham, *Classification of carbonate rocks*. AAPG Memoir 1, 108-121.
- 687 Embry III, A. F., Klovan, J. E., 1971. A late Devonian reef tract on northeastern Banks Island,  
688 NWT. *Bulletin of Canadian Petroleum Geology* 19, 730-781.
- 689 Festa, V., 2003. Cretaceous structural features of the Murge area (Apulian Foreland, southern  
690 Italy). *Eclogae Geologicae Helvetiae* 96, 11-22.

- 691 Flemings, P. B., Jordan, T. E., 1989. A synthetic stratigraphic model of foreland basin  
692 development. *Journal of Geophysical Research: Solid Earth* 94(B4), 3851-3866.
- 693 Flodin, E. A., Aydin, A., 2004. Evolution of a strike-slip fault network, Valley of Fire State  
694 Park, southern Nevada. *Geological Society of America Bulletin* 116, 42-59.
- 695 Foglio I.G.M. 211, S. Arcangelo. Istituto Geografico Militare.
- 696 Fossen, H., Rotevatn, A., 2016. Fault linkage and relay structures in extensional settings-A  
697 review. *Earth-Science Reviews* 154, 14-28.
- 698 Gawthorpe, R. L., Leeder, M. R., 2000. Tectono-sedimentary evolution of active extensional  
699 basins. *Basin Research* 12, 195-218.
- 700 Ghisetti, F., Vezzani, L., 1981. Contribution of structural analysis to understanding the  
701 geodynamic evolution of the Calabrian Arc (Southern Italy). *Journal of Structural Geology* 3,  
702 371-381.
- 703 Ghisetti, F., Vezzani, L., 1997. Interfering paths of deformation and development of arcs in  
704 the fold-and-thrust belt of central Apennines (Italy). *Tectonics* 16, 523-536.
- 705 Grandjacquet, C., 1963. Schéma structural de l'Apennin campano-lucanien (Italie). *Revue de*  
706 *Géographie Physique et de Géologie Dynamique* 25, 185-202.
- 707 Gupta, A., Scholz, C. H., 2000. A model of normal fault interaction based on observations  
708 and theory. *Journal of Structural Geology* 22, 865-879.
- 709 Harding, T. P., Tuminas, A. C., 1989. Structural interpretation of hydrocarbon traps sealed by  
710 basement normal block faults at stable flank of foredeep basins and at rift basins. *AAPG*  
711 *Bulletin* 73, 812-840.
- 712 Holt, W. E., Stern, T. A., 1994. Subduction, platform subsidence, and foreland thrust loading:  
713 The late Tertiary development of Taranaki Basin, New Zealand. *Tectonics* 13, 1068-1092.

- 714 Huggins, P., Watterson, J., Walsh, J. J., Childs, C., 1995. Relay zone geometry and  
715 displacement transfer between normal faults recorded in coal-mine plans. *Journal of*  
716 *Structural Geology* 17, 1741-1755.
- 717 Improta, L., Iannaccone, G., Capuano, P., Zollo, A., Scandone, P., 2000. Inferences on the  
718 upper crustal structure of Southern Apennines (Italy) from seismic refraction investigations  
719 and sub-surface data. *Tectonophysics* 317, 273-297.
- 720 Ippolito, F., D'Argenio, B., Pescatore, T., Scandone, P., 1975. Structural-stratigraphic units  
721 and tectonic framework of Southern Apennines. In SQUYRES C. Ed., *Geology of Italy,*  
722 *Earth Science. Society of Lybian Arabic Republic* 317-328.
- 723 Kim, Y.S., Sanderson, D. J., 2005. The relationship between displacement and length of  
724 faults. *Earth Science Reviews* 68, 317-334.
- 725 Knott, S. D., 1987. The Liguride Complex of southern Italy-a Cretaceous to Paleogene  
726 accretionary wedge. *Tectonophysics* 142, 217-226.
- 727 Korneva, I., Tondi, E., Agosta, F., Rustichelli, A., Spina, V., Bitonte, R., Di Cuia, R., 2014.  
728 Structural properties of fractured and faulted Cretaceous platform carbonates, Murge  
729 Plateau (southern Italy). *Marine and Petroleum Geology* 57, 312-326.
- 730 La Bruna, V., Agosta, F., Prosser, G., 2017. New insights on the structural setting of the  
731 Monte Alpi area, Basilicata, Italy. *Italian Journal of Geosciences*. 136, 220-237.
- 732 Laurita, S., Agosta, F., Cavalcante, F., Rustichelli, A., Giorgioni, M., 2016. Shearing of syn-  
733 sedimentary carbonate breccia along strike-slip faults, Altamura Fm., Southern  
734 Italy. *Italian Journal of Geosciences* 135, 41-54.
- 735 Lentini, F., 1991. *Carta geologica del Bacino del Fiume Agri. Regione Basilicata-*  
736 *Dipartimento Assetto del Territorio. S.EL.CA., Firenze*

- 737 Lentini, F., Carbone, S., Catalano, S., Monaco, C., 2002. Confronti sedimentologico-  
738 petrografici e posizione strutturale dei flysch di Albidona e di Gorgoglione nella media val  
739 d'Agri (Appennino lucano). *Memorie della Società Geologica Italiana* 38, 259-273.
- 740 Locardi, E., 1988. The origin of the Apennine Arcs. *Tectonophysics* 146, 105-123.
- 741 Lorenzo, J. M., O'Brien, G. W., Stewart, J., Tandon, K., 1998. Inelastic yielding and  
742 forebulge shape across a modern foreland basin: North West Shelf of Australia, Timor Sea.  
743 *Geophysical Research Letters* 25, 1455-1458.
- 744 Maerten, L., Willemsse, E. J., Pollard, D. D., Rawnsley, K., 1999. Slip distributions on  
745 intersecting normal faults. *Journal of Structural Geology* 21, 259-272.
- 746 Mallet, J. L., Jacquemin, P., Cheimanoff, N., 1989. GOCAD project: Geometric modeling of  
747 complex geological surfaces, In *SEG Technical Program Expanded Abstracts 1989*.  
748 *Society of Exploration Geophysicists* 126-128.
- 749 Mallet, J. L., 2002. *Geomodeling Oxford University Press*.
- 750 Mandelbrot, B. B., Pignoni, R., 1983. *The fractal geometry of nature (Vol. 173)*. New York:  
751 WH freeman.
- 752 Manighetti, I., King, G. C. P., Gaudemer, Y., Scholz, C. H., Doubre, C., 2001. Slip  
753 accumulation and lateral propagation of active normal faults in Afar. *Journal of*  
754 *Geophysical Research: Solid Earth* 106, 13667-13696.
- 755 Mansfield, C. S., Cartwright, J. A., 1996. High resolution fault displacement mapping from  
756 three-dimensional seismic data: evidence for dip linkage during fault growth. *Journal of*  
757 *Structural Geology* 18, 249-263.
- 758 Marabini, S., Vai, G. B., 1985. Analisi di facies e macrotettonica della vena del gesso di  
759 Romagna. *Bollettino della Società Geologica Italiana* 104, 21-42.
- 760 Massot, J., 2002. Implementation of 3D balanced restoration methods. Ph.D. Dissertation.  
761 *Institut Polytechnique National de Lorraine, Nancy, France, 157 pp.*

- 762 Mazzoli, S., Aldega, L., Corrado, S., Invernizzi, C., Zattin, M., 2006. Pliocene-Quaternary  
763 thrusting, syn-orogenic extension and tectonic exhumation in the southern Apennines  
764 (Italy): Insights from the Alpi Mt. area. In *Styles of Continental Contraction*, edited by S.  
765 Mazzoli and R.W.H. Butler. Geological Society of America 414, 55-77.
- 766 Mazzoli, S., Ascione, A., Buscher, J. T, Pignalosa. A., Valente, E., Zattin, M., 2014. Low-  
767 angle normal faulting and focused exhumation associated with late Pliocene change in  
768 tectonic style in the southern Apennines (Italy). *Tectonics* 33,1802-1818.
- 769 McLeod, A., Dawers, N. H., Underhill, J. R., 2000. The propagation and linkage of normal  
770 faults: insight from the Strathspey-Brent-Statfjord fault array, northern North Sea. *Basin*  
771 *Research* 12, 263-284.
- 772 Medwedeff, D. A., Krantz, R. W., 2002. Kinematic and long modelling of 3-D extensional  
773 ramps: observations and a new 3-D deformation model. *Journal of Structural Geology* 24  
774 763-772.
- 775 Menardi Noguera, A., Rea, G., 2000. Deep structure of the Campanian-Lucanian Arc  
776 (southern Apennines). *Tectonophysics* 324, 239-265.
- 777 Meyer, V., Nicol, A., Childs, C., Walsh, J. J., Watterson, J., 2002. Progressive localisation of  
778 strain during the evolution of a normal fault population. *Journal of Structural Geology* 24,  
779 1215-1231.
- 780 Monaco, C., Tansi, C., 1992. Strutture transpressive lungo la zona trascorrente sinistra nel  
781 versante orientale del Pollino (Appennino calabro-lucano). *Bollettino della Società*  
782 *Geologica Italiana* 111, 291-301.
- 783 Monaco, C., Tortorici, L. 1995). Tectonic role of ophiolitic-bearing terranes in the  
784 development of the Southern Apennine orogenic belt. *Terra Nova* 7, 153-160.
- 785 Monaco, C., Tortorici, L. Paltrinieri, W., 1998. Structural evolution of the Lucanian  
786 Apennines, southern Italy. *Journal of Structural Geology* 20, 617-638.

- 787 Molemma, P. N., Antonellini, M., 1999. Development of strike-slip faults in the Dolomites of  
788 the Sella Group, Northern Italy. *Journal of Structural Geology* 21, 273-292.
- 789 Mostardini, F., Merlini, S., 1986. Appennino centro-meridionale. Sezioni geologiche e  
790 proposta di modello strutturale. *Memorie della Società Geologica Italiana* 35, 177-202.
- 791 Muller, C., Casero, P., Moretti, I., Roure, F., Sage, L., 1988. Significance of the Alpi Mt. in  
792 the geodynamic evolution of the Southern Apennines. *Atti 74<sup>th</sup> Congresso della Società*  
793 *Geologica Italiana B*, 333-335.
- 794 Muraoka, H., Kamata, H., 1983. Displacement distribution along minor fault traces. *Journal*  
795 *of Structural Geology* 5, 483-495.
- 796 Myers, R., Aydin A., 2004. The evolution of faults formed by shearing across joint zones in  
797 sandstones. *Journal of Structural Geology* 26, 947-966.
- 798 Nicol, A., Watterson, J., Walsh, J. J., Childs, C., 1996. The shapes, major axis orientations  
799 and displacement patterns of fault surfaces. *Journal of Structural Geology* 18, 235-248.
- 800 Nicolai, C., Gambini, R., 2007. Structural architecture of the Adria platform-and-basin  
801 system. *Bollettino Società Geologica Italiana* 7, 21-37.
- 802 Ogniben, L., 1969. Schema introduttivo alla geologia del confine calabro-lucano. *Memorie*  
803 *della Società Geologica Italiana* 8, 453-763.
- 804 Oldow, J. S., D'Argenio, B., Ferranti, L., Pappone, G., Marsella, E., Sacchi, M., 1993. Large-  
805 scale longitudinal extension in the southern Apennines contractional belt, Italy. *Geology*  
806 21, 1123-1126
- 807 Ortolani, F., Torre, M., 1971. Il Mt. Alpi (Lucania) nella paleogeografia dell'Appennino  
808 meridionale. *Bollettino della Società Geologica Italiana* 90, 213-248.
- 809 Panza, E., Agosta, F., Zambrano, M., Tondi, E., Prosser, G., Giorgioni, M., Janiseck, J. M.,  
810 2015. Structural architecture and Discrete Fracture Network modelling of layered fractured  
811 carbonates (Altamura Fm., Italy). *Italian Journal of Geosciences* 134, 409-422.

- 812 Panza, E., Agosta, F., Zambrano, M., Tondi, E., Prosser, G., Giorgioni, M., Janiseck, J. M.,  
813 2016. Fracture stratigraphy and fluid flow properties of shallow-water, tight carbonates:  
814 The case study of the Murge Plateau (southern Italy). *Marine and Petroleum Geology* 73,  
815 350-370.
- 816 Patacca, E., Sartori, R., Scandone, P. 1990. Tyrrhenian basin and Apenninic arcs: kinematic  
817 relations since late Tortonian times. *Memorie Società Geologica Italiana* 45, 425-451.
- 818 Patacca, E., Scandone, P., Bellatalla, M., Perilli, N., Santini, U., 1992. The Numidian-sand  
819 event in the Southern Apennines. *Mem. Sci. Geol. Padova* 43, 297-337.
- 820 Patacca, E., Scandone, P., 2007. Geology of southern Apennines. Results of the CROP  
821 Project. Sub-project CROP-04: In: Mazzotti A., Patacca E., Scandone P., (Eds). *Bollettino*  
822 *della Società Geologica Italiana* 7, 75-119.
- 823 Peacock, D.C.P., Sanderson, D. J., 1991. Displacement, segment linkage and relay ramps in  
824 normal fault zones. *Journal of Structural Geology* 13, 721-733.
- 825 Pescatore, T., Renda, P., Schiattarella, M., Tramutoli, M., 1999. Stratigraphic and structural  
826 relationships between Meso-Cenozoic Lagonegro basin and coeval carbonate platforms in  
827 southern Apennines, Italy. *Tectonophysics* 315, 269-286.
- 828 Petrullo, A. V., Agosta, F., Prosser, G., Rizzo, E., 2017. Cenozoic tectonic evolution of the  
829 northern Apulian carbonate platform (southern Italy). *Italian Journal of Geosciences* 136,  
830 296-311.
- 831 Pieri, P., Laviano A., 1989. Tettonica e sedimentazione nei depositi senomiani delle Murge  
832 sud-orientali (Ostuni). *Bollettino della Società Geologica Italiana* 108, 351-356.
- 833 Pieri, P., Festa, V., Moretti, M., Tropeano, M., 1997. Quaternary tectonic activity of the  
834 Murge area (Apulian foreland-Southern Italy). *Annals of Geophysics* 40.

- 835 Plint, A. G., Hart, B. S., Donaldson, W. S., 1993. Lithospheric flexure as a control on stratal  
836 geometry and facies distribution in Upper Cretaceous rocks of the Alberta foreland basin.  
837 Basin Research 5, 69-77.
- 838 Ranero, C.R., Morgan, J.P., McIntosh, K., Reichert, C., 2003. Bending-related faulting and  
839 mantle serpentinization at the Middle America trench. Nature 425, 36-373.
- 840 Roda, C., 1965. Livelli a struttura grumosa e livelli ad ooliti rotte e rigenerate nel calcare  
841 miocenico del Alpi Mt. (Potenza). Geologica Romana 4.
- 842 Royden, L., Patacca, E., Scandone, P., 1987. Segmentation and configuration of subducted  
843 lithosphere in Italy: An important control on thrust-belt and foredeep-basin evolution.  
844 Geology 15, 714-717.
- 845 Royden, L. H., 1993. The tectonic expression slab pull at continental convergent boundaries.  
846 Tectonics 12, 303-325.
- 847 Sartoni, S., Crescenti U., 1962. Ricerche biostratigrafiche nel Mesozoico dell'Appennino  
848 Meridionale. Giornale di Geologia 29, 161-309.
- 849 Schettino, A., Turco E., 2011. Tectonic history of the western Tethys since the late Triassic.  
850 Geological Society of America Bulletin 123, 89-105.
- 851 Shiner, P., Beccacini, A., Mazzoli, S., 2004. Thin-skinned versus thick-skinned structural  
852 models for Apulian Carbonate Reservoirs: constraints from the Val D'Agri Field. Marine  
853 and Petroleum Geology 21, 805-827.
- 854 Schlagenhauf, A., Manighetti, I., Malavieille, J., Dominguez, S., 2008. Incremental growth of  
855 normal faults: Insights from a laser-equipped analog experiment. Earth and Planetary  
856 Science Letters 273, 299-311.
- 857 Schlische, R. W., Young, S. S., Ackermann, R. V, Gupta, A., 1996. Geometry and scaling  
858 relations of a population of very small rift-related normal faults. Geology 24, 683-686.

- 859 Scholz, C. H., Dawers N. H., Yu, J. Z., Anders, M. H., Cowie, P. A., 1993. Fault growth and  
860 fault scaling laws: preliminary results. *Journal of Geophysical Research: Solid Earth* 98,  
861 21951-21961.
- 862 Schultz, R. A., Soliva, R., Fossen, H., Okubo, C. H., Reeves, D. M., 2008. Dependence of  
863 displacement–length scaling relations for fractures and deformation bands on the  
864 volumetric changes across them. *Journal of Structural Geology* 30, 1405-1411.
- 865 Schultz, R. A., Soliva, R., Okubo, C. H., Mege, D., 2010. Fault populations. *Planetary*  
866 *Tectonics* 457-510.
- 867 Segall, P., Pollard D. D., 1980. Mechanics of discontinuous faults. *Journal of Geophysical*  
868 *Research: Solid Earth* 85, 4337-4350.
- 869 Segall, P., Pollard, D. D., 1983. Nucleation and growth of strike slip faults in granite. *Journal*  
870 *of Geophysical Research: Solid Earth* 88, 555-568
- 871 Selli, R., 1957. Sulla trasgressione del Miocene nell'Italia meridionale. *Giornale Di Geologia*  
872 2, 26-54.
- 873 Sgrosso, I., 1988. Nuovi dati biostratigrafici sul Miocene del M. Alpi (Lucania) e conseguenti  
874 ipotesi paleogeografiche. *Memorie della Società Geologica Italiana* 41, 343-351.
- 875 Spalluto, L., 2012. Facies evolution and sequence chronostratigraphy of a “mid”-Cretaceous  
876 shallow-water carbonate succession of the Apulia Carbonate Platform from the northern  
877 Murge area (Apulia, southern Italy). *Facies* 58, 17-36.
- 878 Taddei, A., Siano, M. G., 1992. Analisi biostratigrafica e considerazioni paleoecologiche sulla  
879 successione neogenica del Alpi Mt. (Lucania). *Bollettino della Società Geologica Italiana*  
880 111, 255-272.
- 881 Tavani, S., Carola E., Granado, P., Quintà, A., Muñoz, J. A., 2013. Transpressive inversion of  
882 a Mesozoic extensional forced fold system with an intermediate décollement level in the  
883 Basque-Cantabrian Basin (Spain). *Tectonics* 32, 146-158.

- 884 Tavani, S., Storti, F., Lacombe, O., Corradetti, A., Muñoz, J. A. Mazzoli, S., 2015a. A review  
885 of deformation pattern templates in foreland basin systems and fold-and-thrust belts:  
886 Implications for the state of stress in the frontal regions of thrust wedges. *Earth Sciences*  
887 *Reviews* 141, 82-104.
- 888 Tavani, S., Vignaroli, G., Parente, M., 2015b. Transverse versus longitudinal extension in the  
889 foredeep-peripheral bulge system: Role of Cretaceous structural inheritances during early  
890 Miocene extensional faulting in inner central Apennines belt. *Tectonics* 34, 1412-1430.
- 891 Tavarnelli, E., Decandia, F.A., Alberti A., 1999. Evidenze di tettonica distensiva  
892 sinsedimentaria nel Bacino messiniano della Laga: implicazioni per l'evoluzione  
893 dell'Appennino Settentrionale. *Bollettino della Società Geologica Italiana*, 118, 2, 217-  
894 227.
- 895 Tavarnelli, E., Pasqui, V., 2000. Fault growth by segment linkage in seismically active  
896 settings: examples from the Southern Apennines, Italy, and the Coast Ranges, California.  
897 *Journal of Geodynamics*, 29, 501-516.
- 898 Tavarnelli, E., Prosser, G., 2003. The complete Apennines orogenic cycle preserved in a  
899 transient single outcrop near San Fele, Lucania, Southern Italy. *Journal of the Geological*  
900 *Society of London*, 160, 429-434.
- 901 Torabi, A., Berg, S. S., 2011. Scaling of fault attributes: A review. *Marine and Petroleum*  
902 *Geology* 28, 1444-1460.
- 903 Trudgill, B., Cartwright, J., 1994. Relay-ramp forms and normal-fault linkages, Canyonlands  
904 National Park, Utah. *Geological Society of America Bulletin* 106, 1143-1157.
- 905 Vai, G.B., Martini, I. P., 2001. Basement and early (pre-Alpine) history. In Vai, G. B.,  
906 Martini, I. P., Eds., *Anatomy of an Orogen: The Apennines and Adjacent Mediterranean*  
907 *Basins*. Kluwer Academic Publication 121-150.

- 908 Van Dijk, J. P., Okkes, F. W. M., 1990. The analysis of shear zones in Calabria: implications  
909 for the geodynamics of the Central Mediterranean. *Rivista Italiana di Paleontologia e*  
910 *Stratigrafia* 96, 241-270.
- 911 Van Dijk, J. P., Bello, M., Toscano, C., Bersani, A., Nardon, S., 2000. Tectonic model and  
912 three-dimensional fracture network analysis of Alpi Mt. (southern Apennines).  
913 *Tectonophysics* 324, 203-237.
- 914 Vitale, S., Dati, F., Mazzoli, S., Ciarcia, S., Guerriero, V., Iannace, A. 2012. Modes and  
915 timing of fracture network development in poly-deformed carbonate reservoir analogues,  
916 Mt. Chianello, southern Italy. *Journal of Structural Geology* 37, 223-235.
- 917 Vitale, S., Ciarcia, S., 2013. Tectono-stratigraphic and kinematic evolution of the  
918 southern Apennines/Calabria–Peloritani Terrane system (Italy). *Tectonophysics* 583, 164-  
919 182.
- 920 Vitale, S., Amore, O. F., Ciarcia, S., Fedele, L., Grifa, C., Prinzi, E. P., Tavani, S.,  
921 Tramparulo, F. D. A., 2017. Structural, stratigraphic, and petrological clues for a  
922 Cretaceous–Paleogene abortive rift in the southern Adria domain (southern Apennines,  
923 Italy). *Geological Journal* DOI: 10.1002/gj.2919.
- 924 Walsh, J. J., Watterson, J., 1987. Distributions of cumulative displacement and seismic slip on  
925 a single normal fault surface. *Journal of Structural Geology* 9(8), 1039-1046.
- 926 Walsh, J. J., Watterson, J., 1988. Analysis of the relationship between displacements and  
927 dimensions of faults. *Journal of Structural Geology* 10, 239-247.
- 928 Walsh, J. J., Watterson, J., 1990. New methods of fault projection for coalmine planning.  
929 *Proceedings of the Yorkshire Geological Society* 48, 209-219.
- 930 Walsh, J. J., Nicol, A., Childs, C., 2002. An alternative model for the growth of faults. *Journal*  
931 *of Structural Geology* 24, 1669-1675.

- 932 Walsh, J. J., Bailey, W. R., Childs, C., Nicol, A., Bonson, C. G., 2003. Formation of  
 933 segmented normal faults: a 3-D perspective. *Journal of Structural Geology* 25, 1251-1262.
- 934 Watterson, J., 1986. Fault dimensions, displacements and growth. *Pure and Applied*  
 935 *Geophysics* 124(1-2), 365-373.
- 936 Whitaker, A. E., Engelder, T., 2006. Plate-scale stress fields driving the tectonic evolution of  
 937 the central Ouachita salient, Oklahoma and Arkansas. *Geological Society of America*  
 938 *Bulletin* 118, 710-723.
- 939 Zhao, M., Jacobi, R. D., 1997. Formation of regional cross-fold joints in the northern  
 940 Appalachian Plateau. *Journal of Structural Geology* 19, 817-834.

941

942 **Figure caption**

943

944 **Figure 1.** Simplified geological map of the Southern Apennines, Italy, and NE-SW  
 945 geological cross section (from *Vitale and Ciarcia, 2013*, and references therein). Location of  
 946 the study area of Monte Alpi is shown both in the geological map and in the inset figure.

947

948 **Figure 2. (a)** Geological map of the Monte Alpi area, and surrounding regions, at a 1:25.000  
 949 scale. Data after original field survey and available bibliography (*Foglio IGM 211, S.*  
 950 *Arcangelo; Bonardi et al., 2009; Cavalcante et al., 2009; Lentini, 1991*). **(b)** Location of the  
 951 sites of stratigraphic logging analysis; **(c)** Traces of the main faults pertaining to the Monte  
 952 Alpi structural network.

953

954 **Figure 3.** Original and interpreted seismic reflection profiles available for the study area.  
 955 Traces of individual seismic profiles are reported in Figure 2. Interpreted sections show the  
 956 main structural features crosscutting the Apulian Platform and allochthonous units.  
 957 Interpretation of stratigraphic horizons and both low-angle and high-angle faults are based on  
 958 available well log data.

959

960 **Figure 4. (a)** Modelled fault surface view due to west. Grey lines represent points with  
 961 similar amounts of throw present along the fault surface, whereas dashed lines show the cut-  
 962 off of the bottom Lower-Cretaceous, Early Messinian and Late Messinian surfaces. **(b)** Throw  
 963 profile computational process on the F1 Fault.

964

965 **Figure 5. (a)** Panoramic view of the western edge of Monte Alpi. There, Mesozoic platform  
 966 carbonates are overlain by two Messinian sedimentary intervals. The lower interval is made  
 967 up of ramp limestones, whereas the upper one includes shallow-marine siliclastics. **(b to g)**  
 968 Photomicrographs of representative samples of the Mesozoic platform carbonates. **(h, i)**  
 969 Outcrop view of a portion of the Monte Alpi western cliff, along which a ENE-WSW striking,  
 970 Early Cretaceous, syn-sedimentary normal fault is exposed.

971

972 **Figure 6.** (a) Panoramic view of the western edge of the Monte Santa Croce peak (cf. Figure  
 973 2). (b to g) Photomicrographs of representative samples of the Lower Messinian carbonates.  
 974 (h and i) Outcrop view and line-drawing of a ENE-WSW striking, Early Messinian, syn-  
 975 sedimentary normal fault.

976

977 **Figure 7.** (a) Outcrop view of the Solarino site (western edge of Monte Alpi). There, the  
 978 Upper Messinian conglomerates form an onlap geometry with respect to the NNW-SSE  
 979 striking F11 Fault, which is therefore interpreted as Late Messinian in age. (b) North-eastern  
 980 edge of the Monte Santa Croce Peak (cf. Figure 2). There, the Upper Messinian sandstones  
 981 and conglomerates form a down-lap geometry with respect to the erosional surface topping  
 982 the Lower Messinian carbonates. (c) Close up view of the Solarino site, where flattened-  
 983 polygenic conglomerates pertaining to the Upper Messinian deposit are exposed. (d) outcrop  
 984 view of the Canale del Grillone site (western sector), where Upper Messinian laminated  
 985 sandstones crop out.

986

987 **Figure 8.** Stratigraphic logs measured across the exposed sections of the Messinian mixed  
 988 carbonates/terrigenous deposits. The location of each log is reported in Figure 2.

989

990 **Figure 9.** (a) Isopach map computed for the Upper Messinian terrigenous deposit. Data are  
 991 reported in meters. White lines represent the traces of the modelled Monte Alpi simplified  
 992 fault network. (b) Lower hemisphere, equal area projections of both poles and planes related  
 993 to unrestored and restored bottom Late Messinian surfaces. Bedding plane data were gathered  
 994 in the field from both western (Canale del Grillone) and eastern (Santa Croce) sectors of  
 995 Monte Alpi. The cartoons show the unrestored and restored geological cross-sections  
 996 elaborated for the study area. Data were restored according to the attitude of Upper Messinian  
 997 beds.

998

999 **Figure 10.** (a) Simplified traces of the Monte Alpi fault network. Dashed lines represent the  
 1000 traces of blind faults. Blue labels are assigned to the faults that are used for throw analysis.  
 1001 (b) Histograms showing both azimuth and dip variations computed for the F1 Fault surface.  
 1002 Both histograms describe the mean of the azimuth/dip value. (c) Snapshot of the 3D  
 1003 geological reconstruction, where the bottom Early Cretaceous surface, F1 Fault, and original  
 1004 geological map are shown.

1005

1006 **Figure 11.** (a) Outcrop view of the N-S striking F1 Fault, which bounds the north-western  
 1007 edge of Monte Alpi. The fault crosscut Jurassic carbonates, and it is characterized by both  
 1008 dip-slip and oblique-slip, extensional kinematics. (b, c) Close up of the F1 Fault. Kinematic  
 1009 indicators, such as calcite fibers and abrasion striae, are visible along the main slip surface.  
 1010 (d) E-W striking, F3 Fault juxtaposing the Monte La Spina dolostones against Lower  
 1011 Cretaceous carbonate. The inset shows the polished slickenside, in which with dip-slip striae  
 1012 are visible. (e) Outcrop view of the F10 fault, which crosscut Lower Messinian carbonates.  
 1013 The inset shows the small veneer of cataclasites present along the polished slickenside;

1014

1015 **Figure 12.** Cumulative throw profiles computed for the 12 major faults pertaining to the  
 1016 Monte Alpi network, in which are present faults with different shape regarding the computed  
 1017 throw profiles (symmetric, bell-shaped, flat-topped and asymmetric profiles). See text for  
 1018 explanation.

1019

1020 **Figure 13.** Pre-Messinian (blue), Early Messinian (green), and post-Early Messinian (yellow)  
1021 throw profiles computed for the 12 major faults pertaining to the Monte Alpi network. See  
1022 text for explanation.

1023

1024 **Figure 14.** Log-Log plots of displacement vs. length data computed for (a) pre-Messinian  
1025 faults ( $y=0.07x^{0.9}$ ;  $R^2=0.42$ ), (b) Early Messinian faults ( $y=0.06x^{0.8}$ ;  $R^2=0.86$ ), and (c) post-  
1026 Early Messinian faults ( $y=0.08x^{1.5}$ ;  $R^2=0.71$ ). (d) Cartoons showing the main stages of fault  
1027 growth, and their related log displacement/ log length data, according to *Cartwright et al.*  
1028 (1995). (e) Cartoons showing both T and Y-shaped intersections for some of the studied  
1029 faults.

1030

1031 **Figure 15.** Time/space evolutionary model proposed for the Monte Alpi foreland basin  
1032 system. The faults active during the main tectonic stages are illustrated in the 3D block  
1033 diagrams, in which the geometry of the sedimentary depocenters is also reported.

1034

1035 **Table 1.** Results of fault analysis performed on the 27 faults used for the 3D geological  
1036 reconstruction. The 75, 50, and 25 percentile distributions of both dip azimuth and dip angle  
1037 computed for the individual faults are shown, respectively. The two main clusters of dip  
1038 azimuth values are computed on the basis of the obtained histograms (ie. Figure 10b), in order  
1039 to decipher the possible horizontal veering of the modelled 3D fault surfaces. In fact, the  
1040 amount of strike variation reported in the last column is related to the difference between the  
1041 two clusters computed, along a horizontal plane, for each modelled fault.

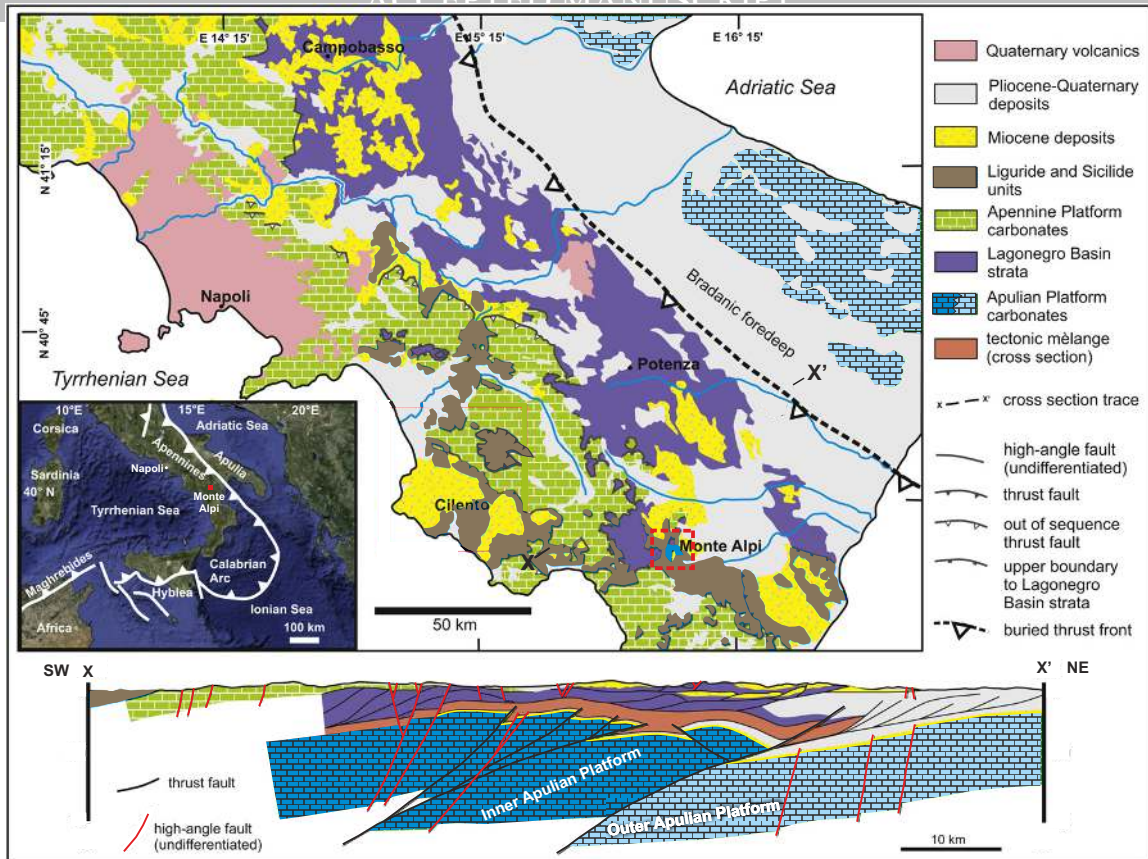
1042

1043 **Table 2.** Name, length and vertical throw of the computed fault segments related to the Pre-  
1044 Messinian (blue), Early Messinian (green), and post-Early Messinian (yellow) structural  
1045 network.

**Figure 6.** (a) Panoramic view of the western edge of the Monte Santa Croce peak (cf. Figure 2). (b to g) Photomicrographs of representative samples of the Lower Messinian carbonates. (h and i) Outcrop view and line-drawing of a ENE-WSW striking, Early Messinian, syn-sedimentary normal fault.

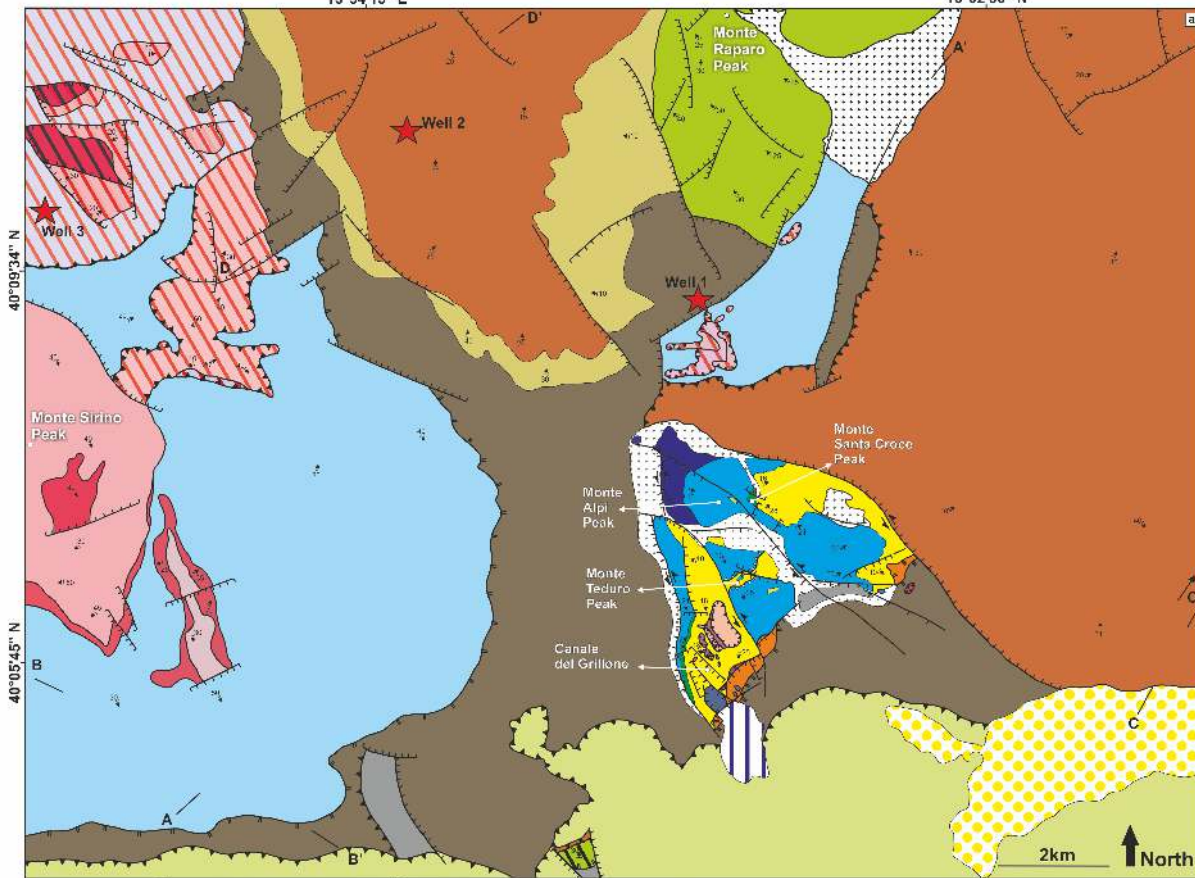
NAME	SET	DIP AZIMUTH 75%	DIP AZIMUTH 50%	DIP AZIMUTH 25%	DIP ANGLE 75%	DIP ANGLE 50%	DIP ANGLE 25%	DIP AZIMUTH CLUSTER 1	DIP AZIMUTH CLUSTER 2	STRIKE VARIATION
F1	II	254.1	248.6	237.9	88.5	85.1	80.7	254	75	1°
F2	I	234.7	194.4	35.7	88.9	87.4	85	235	35	20°
F3	III	319.3	315.9	191.7	86.1	83.5	78.8	320	135	5°
F4	I	228.4	58.5	52.4	88	84.4	75.4	225	60	15°
F5	I	223.5	202.2	42.8	89	87.6	85.4	235	40	15°
F6	III	342	336.5	323	77.6	74.1	69.2	345	/	/
F7	III	159.1	157.2	155.5	79.8	73.5	67.9	/	/	/
F8	III	155.3	155.1	154.9	89.1	88.3	87.9	/	/	/
F9	I	38.6	29.3	25.5	68.1	65.4	64.1	/	/	/
F10	IV	203.1	23.3	22.5	89.6	89.3	87.6	204	23	1°
F11	II	76.9	74.1	70	87.4	85.6	81.5	70	260	10°
F12	III	344.8	188.9	180.4	87.3	83.6	81.5	170	345	5°
F13	I	228.6	227.5	223.5	87.5	86.1	84.4	/	/	/
F14	V	187	12.7	8.6	89	88.3	87.5	180	8	8°
F15	IV	97.1	89.4	76.5	61.4	59	55.7	/	/	/
F16	IV	107.2	92.8	77.3	65.8	64	62.7	/	/	/
F17	II	76.2	72.5	68.9	74.2	67.7	62.3	/	/	/
F18	II	75.9	70.5	66.9	71.7	64.4	58.8	/	/	/
F19	I	226.1	225.1	224	78.2	77.4	75.6	/	/	/
F20	V	112.2	109.3	108.1	79.6	78.6	76.8	/	/	/
F21	V	19.7	17.9	13.8	73.9	72.2	71.1	/	/	/
F22	III	325.7	319.8	307.3	85.3	81.5	77.5	/	/	/
F23	II	251.4	249.7	245.8	87.5	86.8	85.9	/	/	/
F24	IV	193	249.7	12.7	88.2	86.7	84.2	193	20	7°
F25	IV	104.9	103.3	102.7	87.7	86.7	86	/	/	/
F26	III	344.5	14.4	10.6	87	83.7	78.3	/	/	/
F27	L.A.N.F.	135.2	86.3	53.6	25.5	22.4	18	/	/	/

	NAME	LENGTH (km)	VERTICAL FAULT THROW (km)
P.M.	F1a	4	0,5
	F1b	3,5	0,6
	F2a	4,2	0,2
	F2b	3,5	0,45
	F3	4	0,15
	F4	1,5	0,05
	F5a	2	0,1
	F5b	1,5	0,08
	F7a	0,6	0,1
	F7b	0,6	0,15
	F8	1,5	0,07
	F9	2,5	0,25
E.M.	F3	1,5	0,1
	F5	4	0,15
	F12	1	0,05
P.E.M.	F1	6,2	0,9
	F2a	3	0,6
	F2b	4	1,4
	F2c	2	0,25
	F3	4,5	0,8
	F4	4,8	0,5
	F5	4	0,5
	F6	1,2	0,2
	F7	1	0,25
	F8	1,8	0,16
	F9	3	0,15
	F10	1	0,02
F11a	0,6	0,02	
F11b	0,8	0,07	
F12	1,6	0,2	

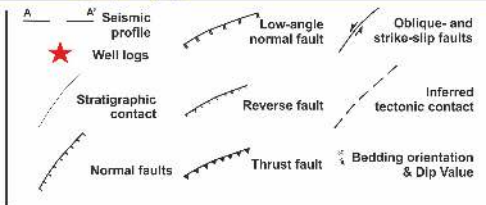
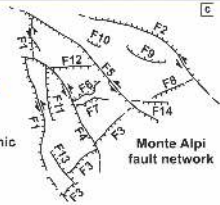


15°54'13" E

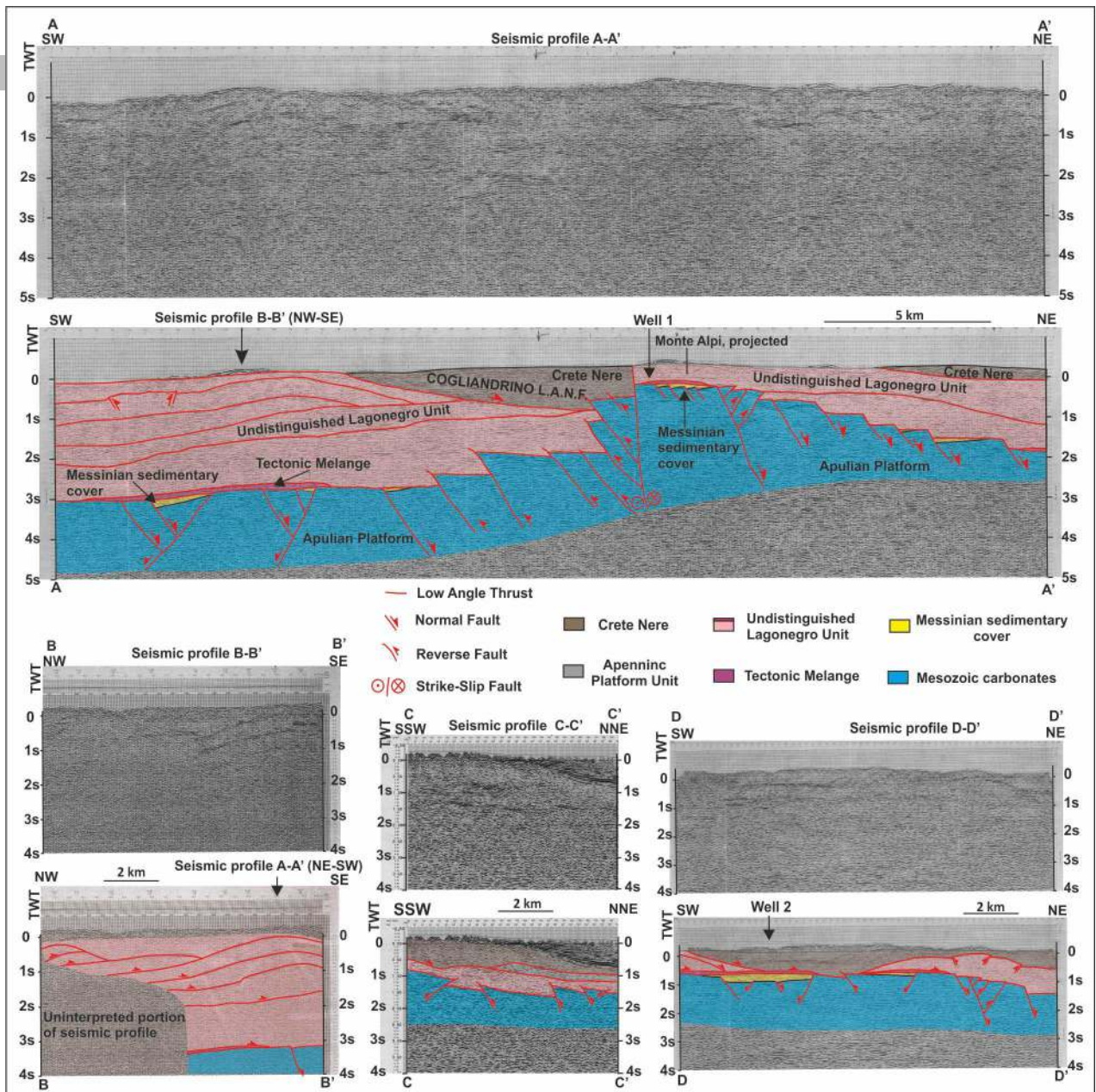
16°02'00" N

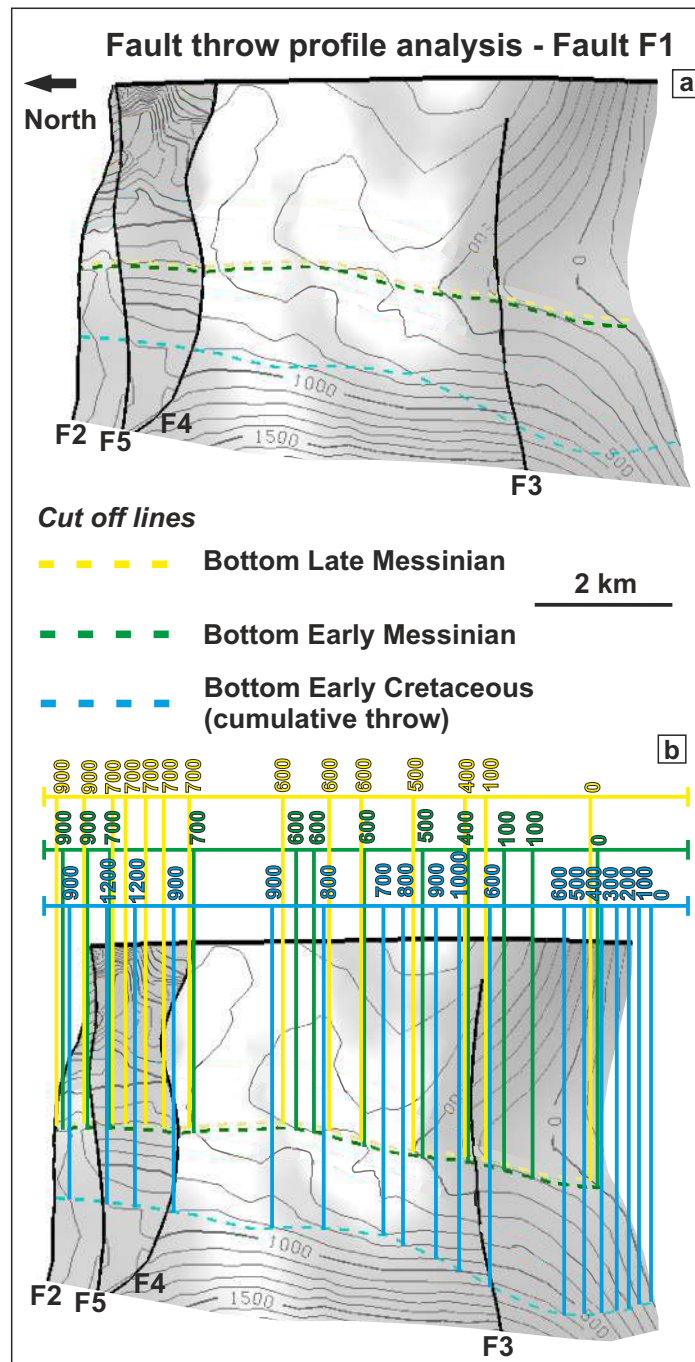


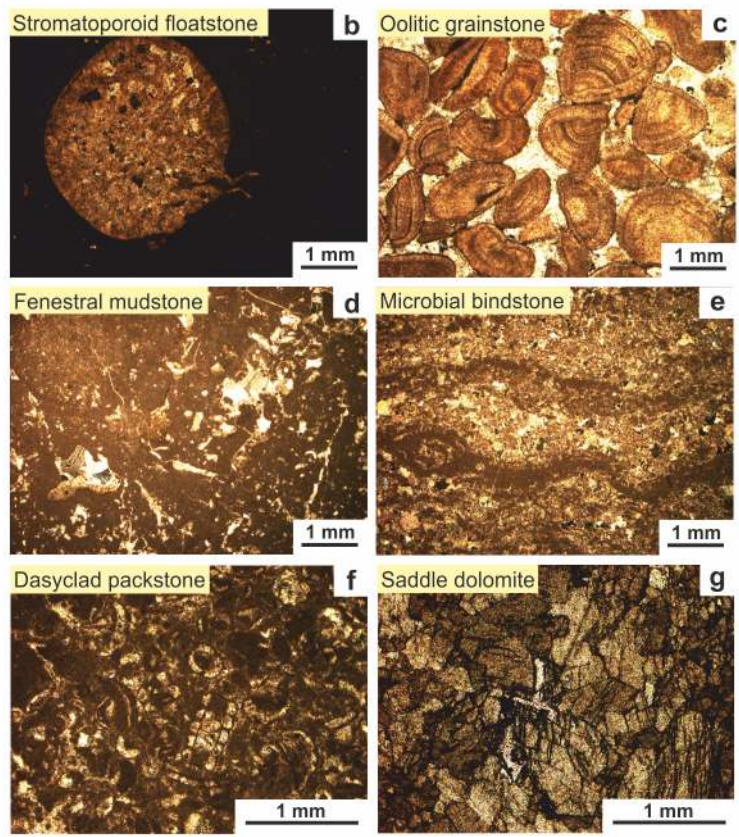
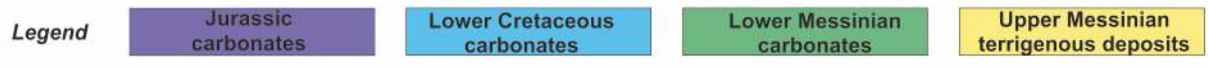
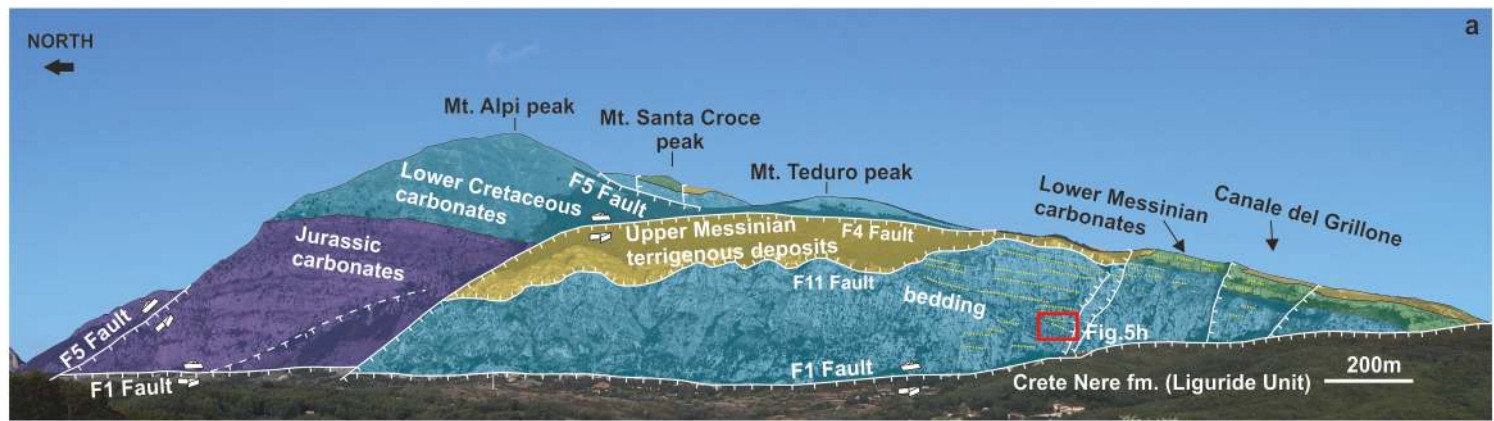
- Debris
- Travertine deposits
- Latronico conglomerates
- Albidona Flysch
  
- LIGURIDE UNIT**
- Saraceno Formation (Upper Oligocene- Lower Miocene)
- Frido Unit (Upper Jurassic- Upper Oligocene)
- Crete Nere (Lower Cretaceous-Middle Eocene)
  
- APENNINIC PLATFORM UNIT**
- Bifurto Formation (Langhian)
- Trenitara Formation (Paleocene-Eocene)
- Monte Raparo Limestones (Upper Cretaceous)
- Monte La Spina Dolostones (Upper Triassic)
  
- LAGONEGRO 2 UNIT**
- Galestrino Flysch 2 (Lower Cretaceous)
- Scisti silicei Formation 2 (Jurassic)
- Cherty limestones 2 (Upper Triassic)
- Monte Facito formation (Lower-Middle Triassic)
  
- LAGONEGRO 1 UNIT**
- Galestrino Flysch 1 (Lower Cretaceous)
- Scisti silicei Formation 1 (Jurassic)
- Cherty limestones 1 (Upper Triassic)
- Bagni Limestones (Upper Triassic)
- Zia Santa (Upper Triassic)
- Tectonic Melange



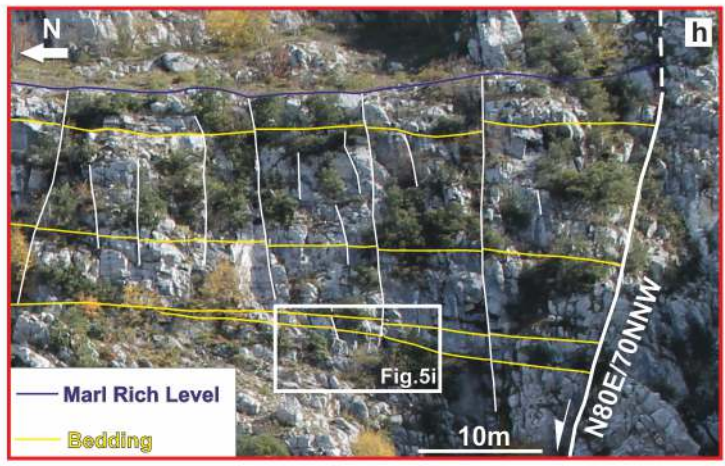
- MONTE ALPI UNIT**
- Upper Messinian terrigenous deposits
- Lower Messinian carbonates
- Lower Cretaceous carbonates
- Jurassic carbonates

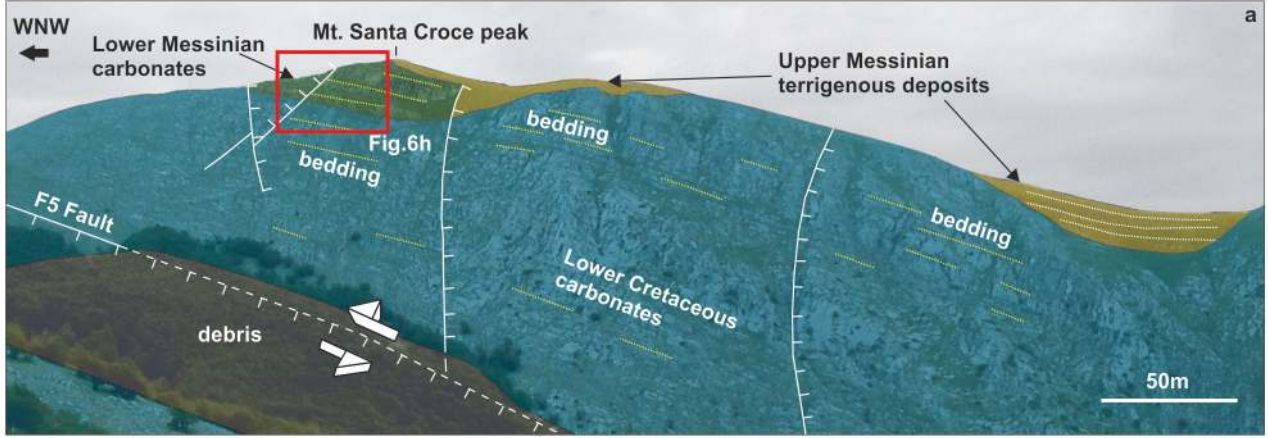






(b-f) = cross-polarized light; (g) = plane-polarized light

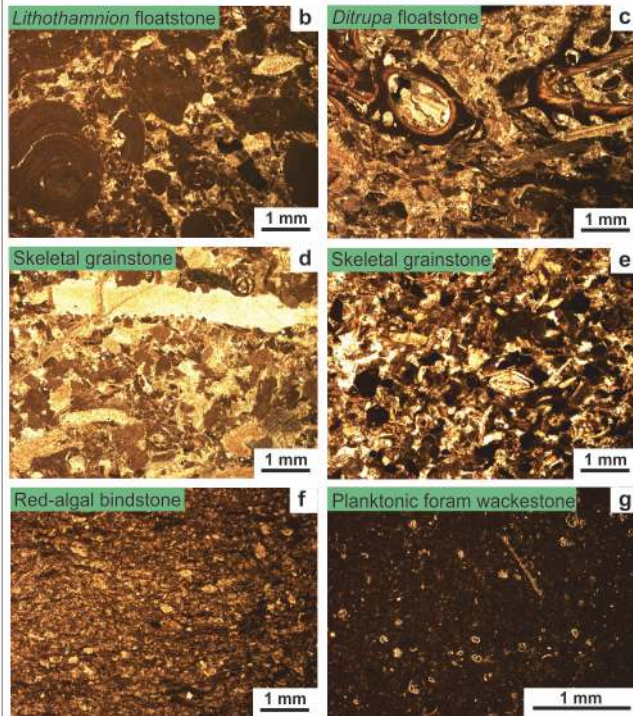




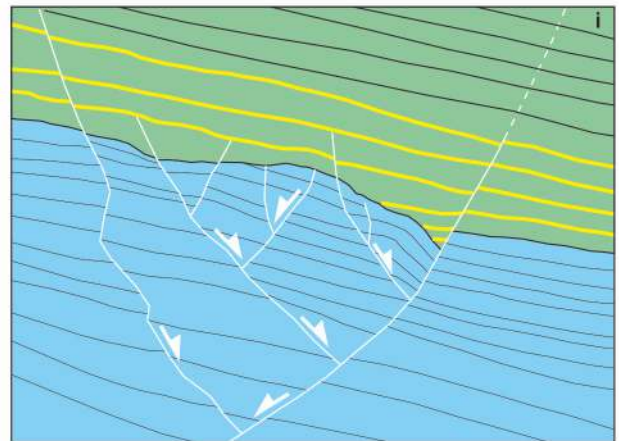
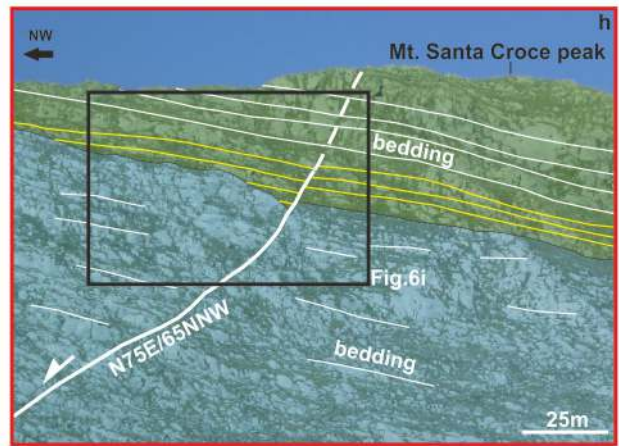
**Legend**

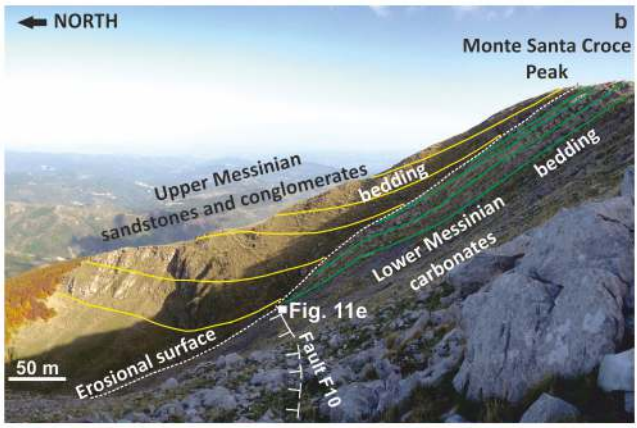
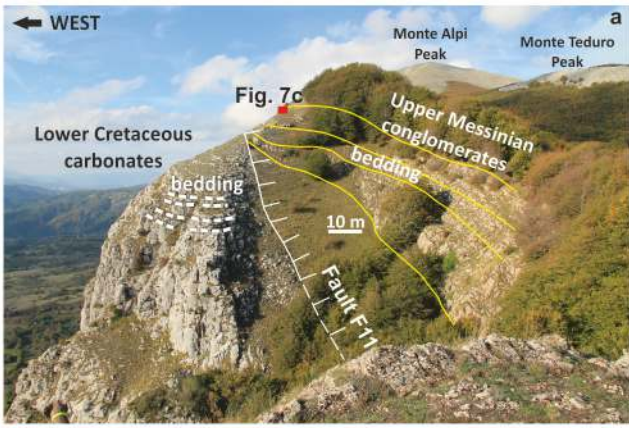
- Lower Cretaceous carbonates
- Lower Messinian carbonates
- Upper Messinian terrigenous deposits

**Lower Messinian carbonates optical microscopical analysis**



(b-f) = cross-polarized light; (g) = plane-polarized light



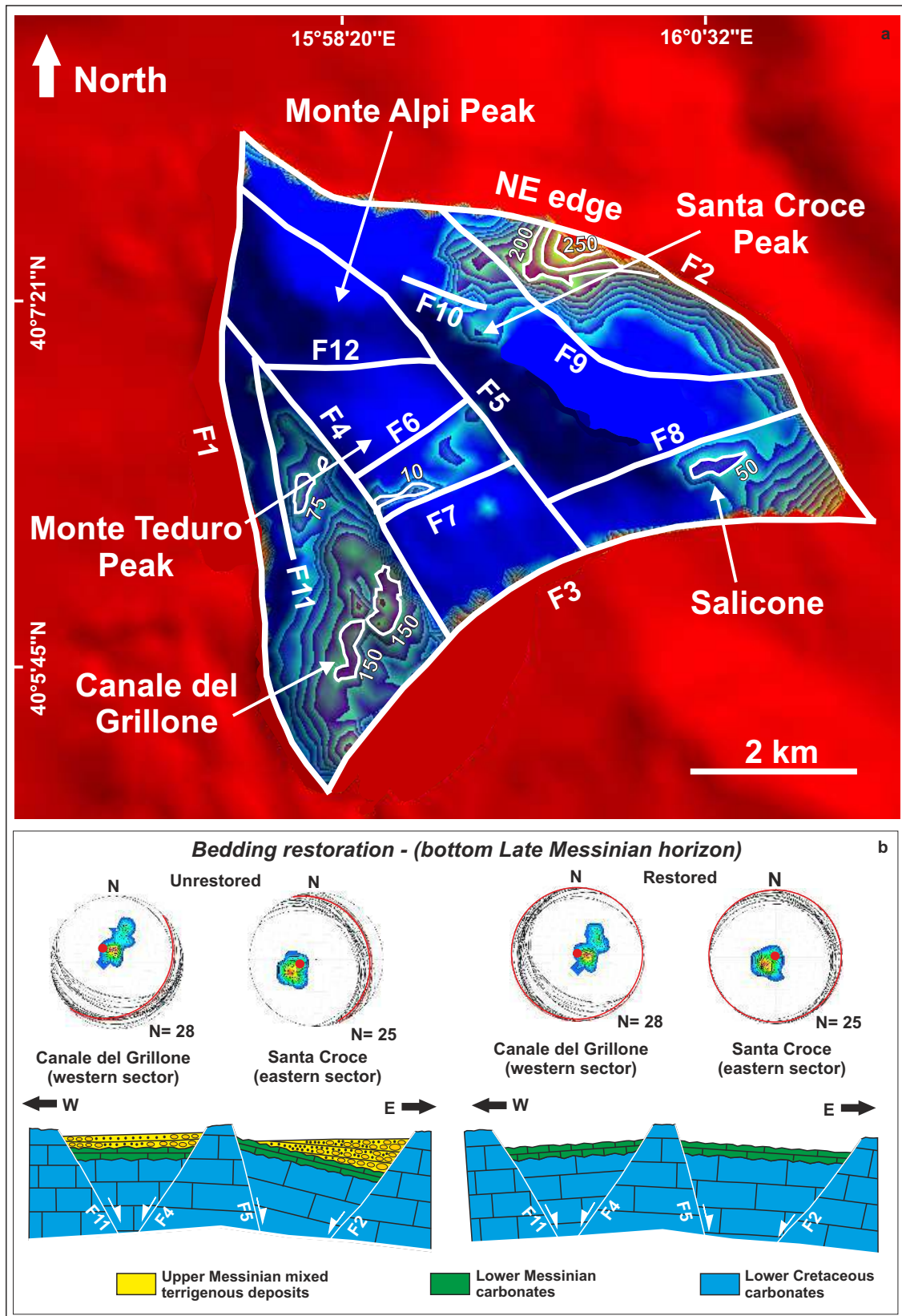


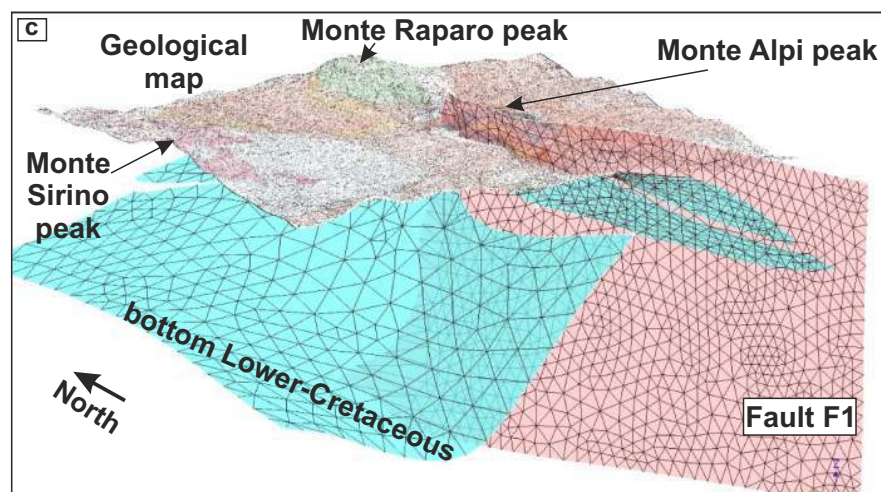
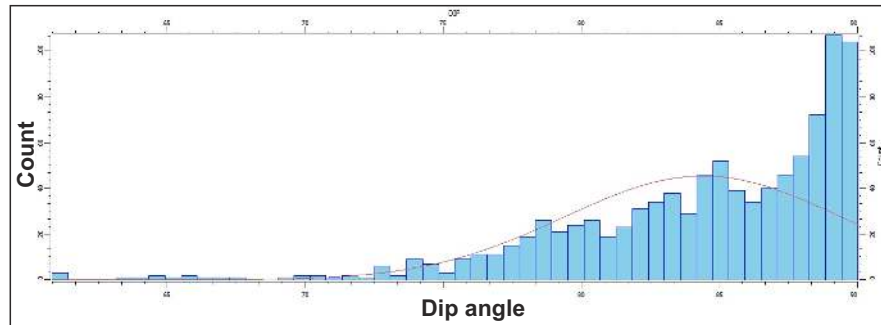
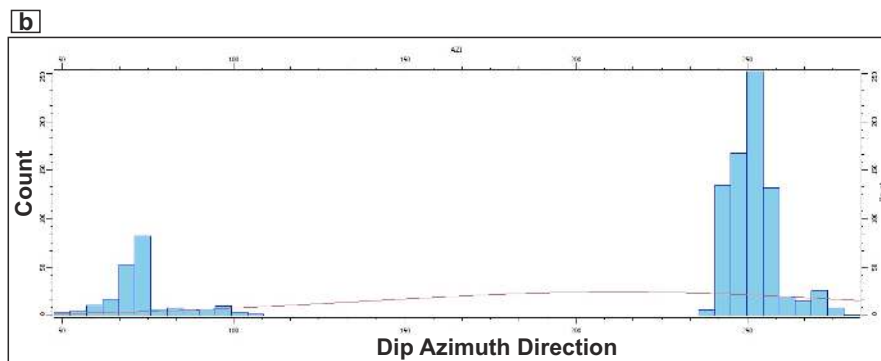
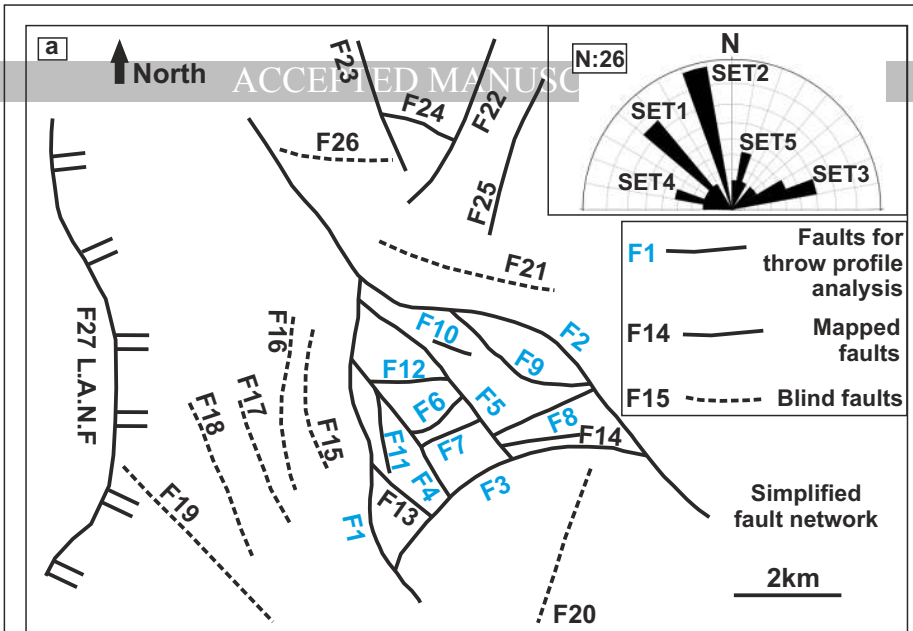
Conglomerates

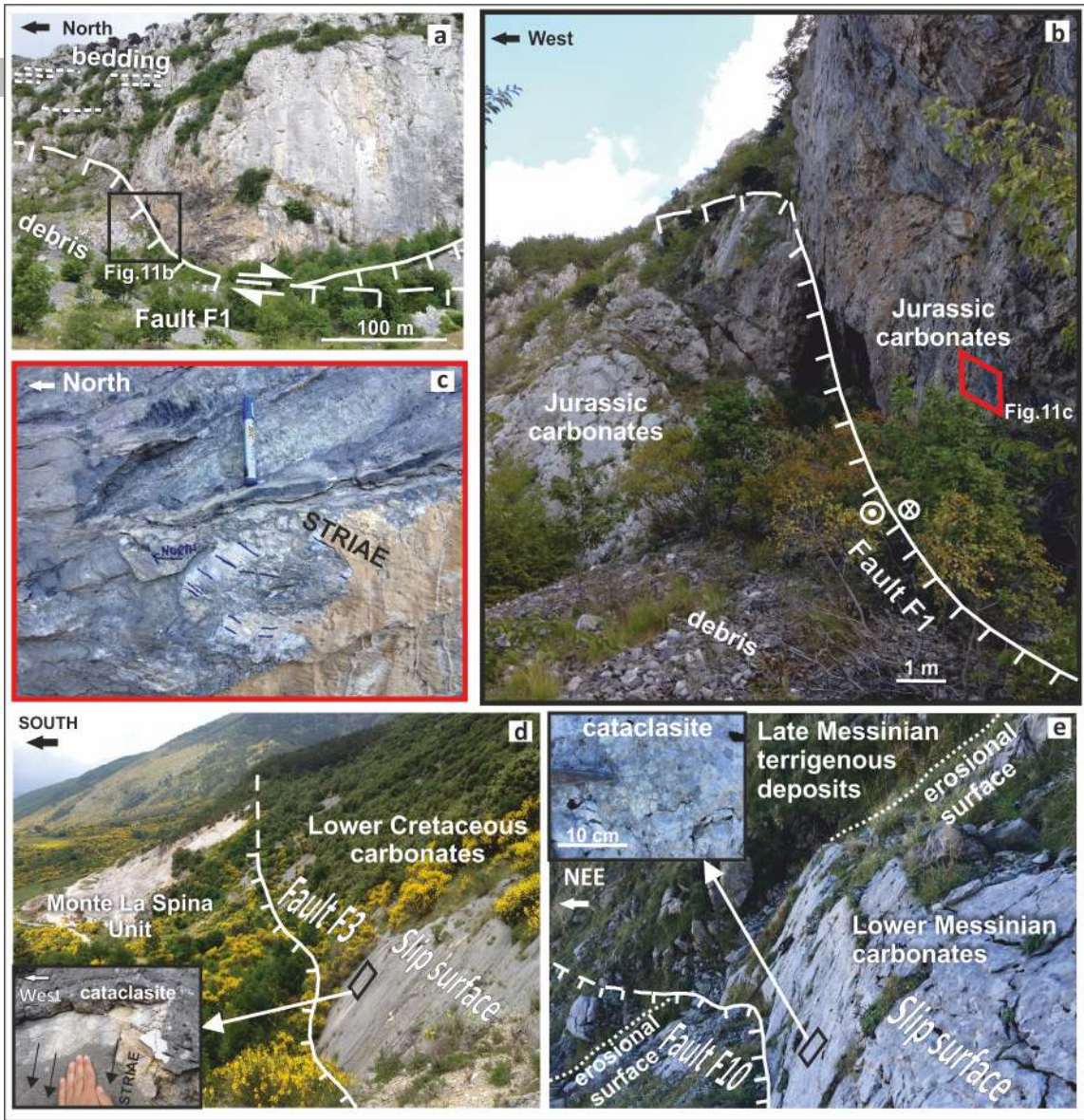


Sandstones

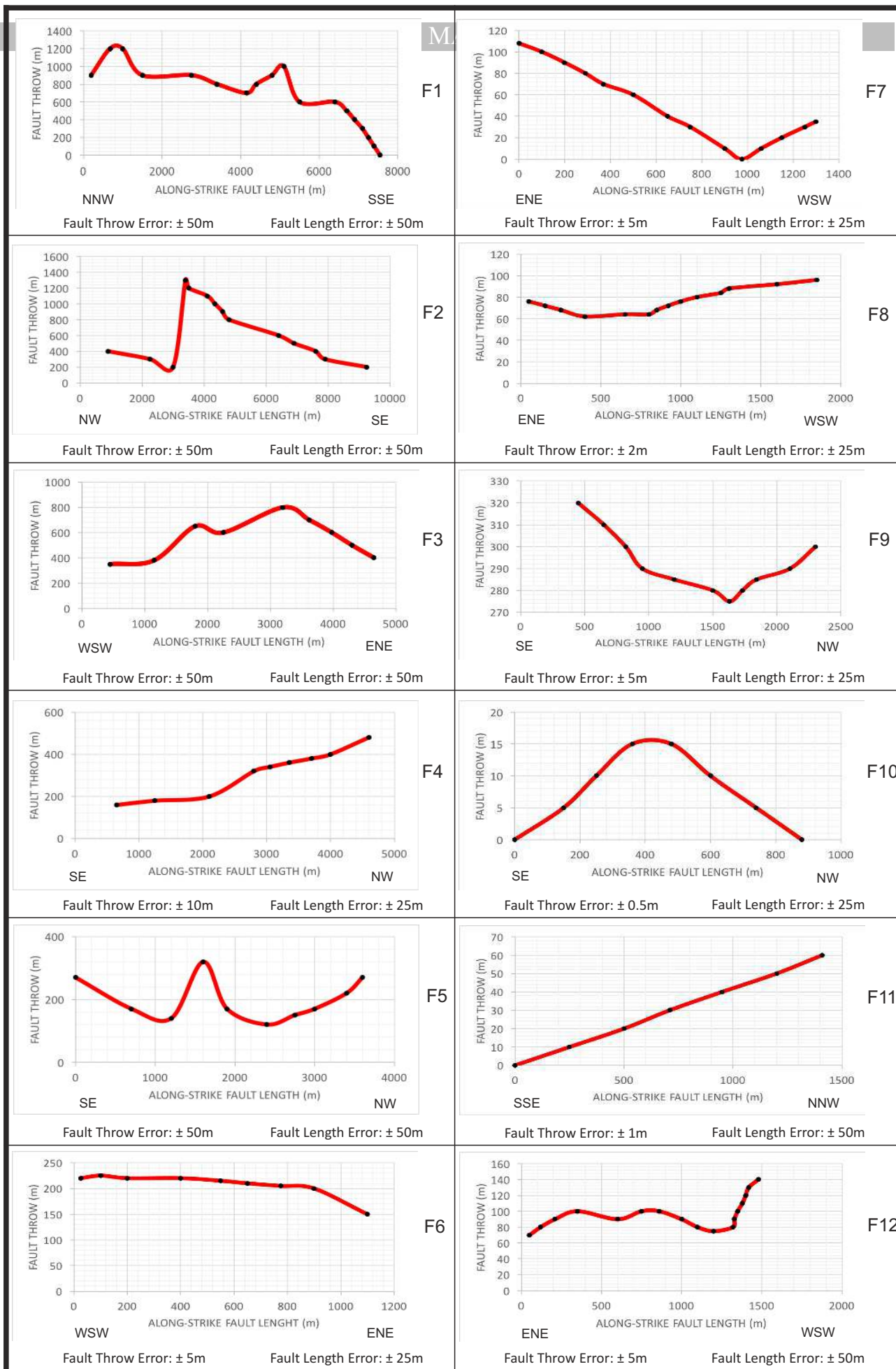




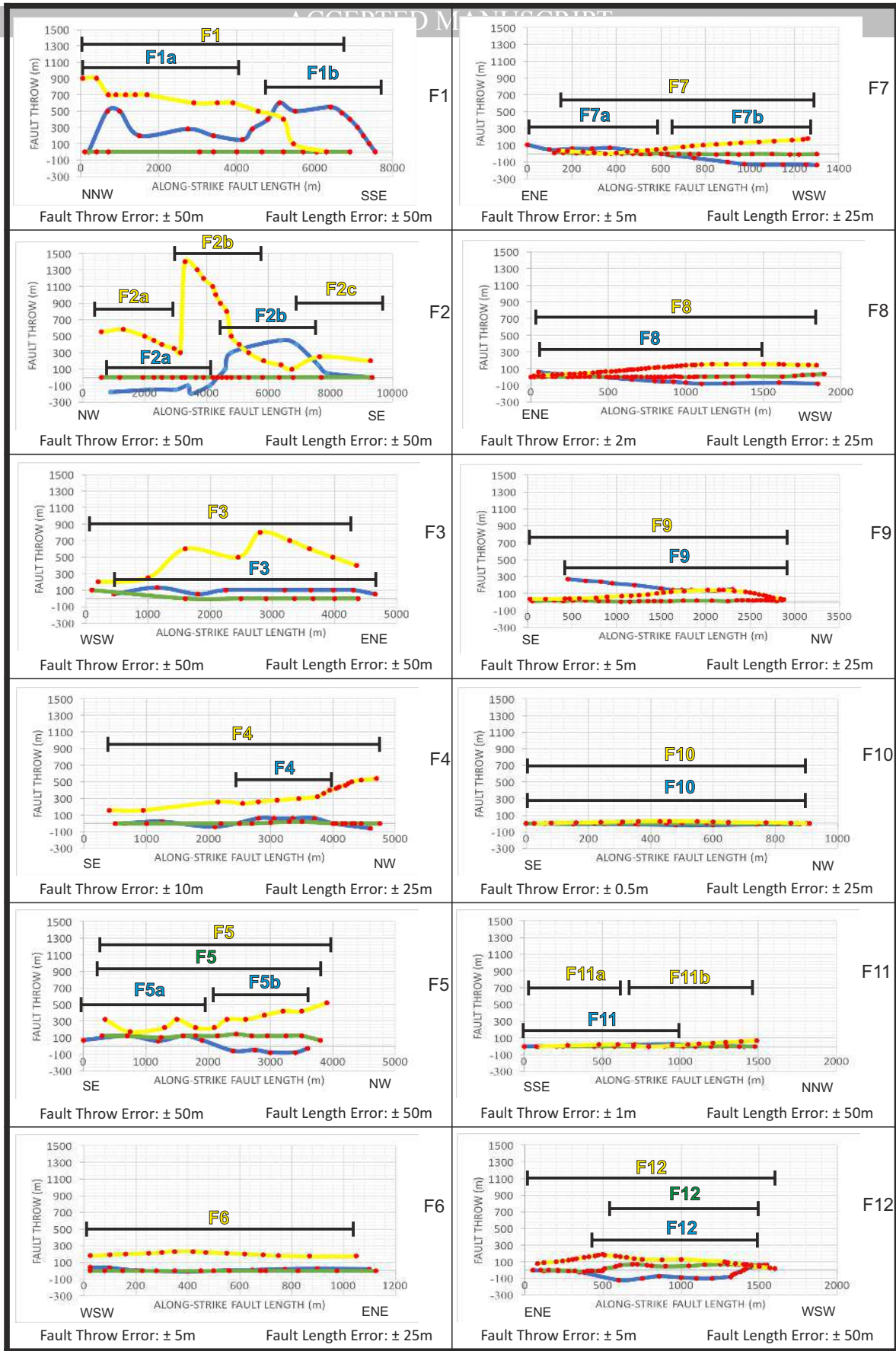


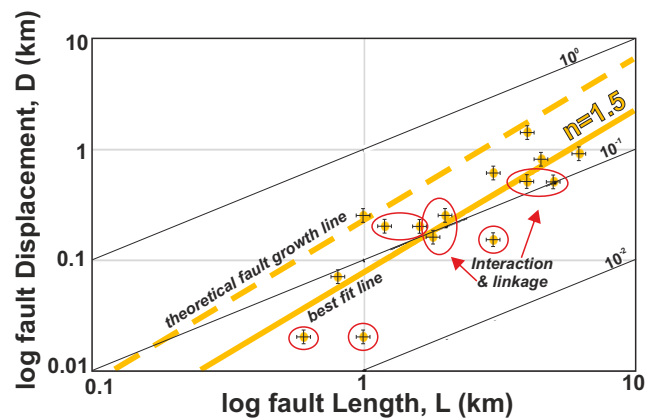
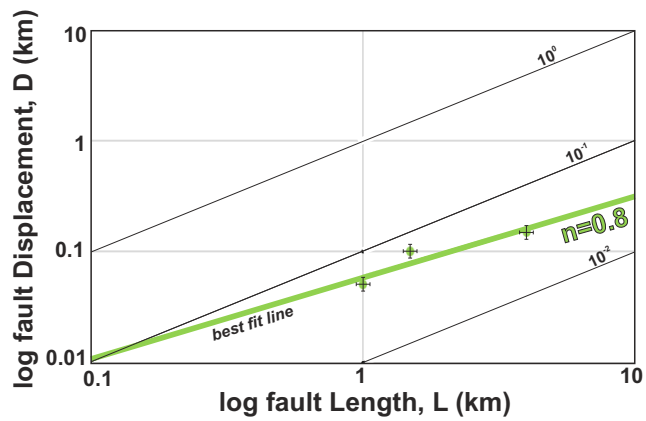
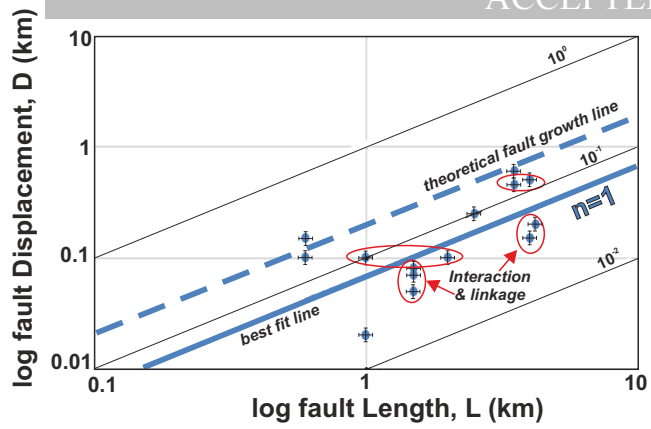


# CUMULATIVE THROW PROFILES

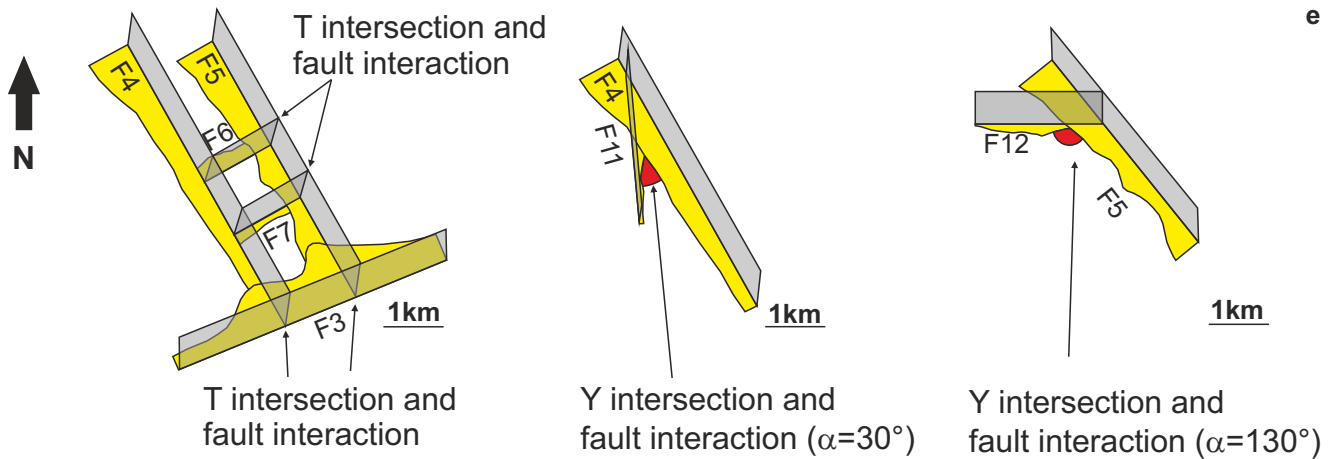
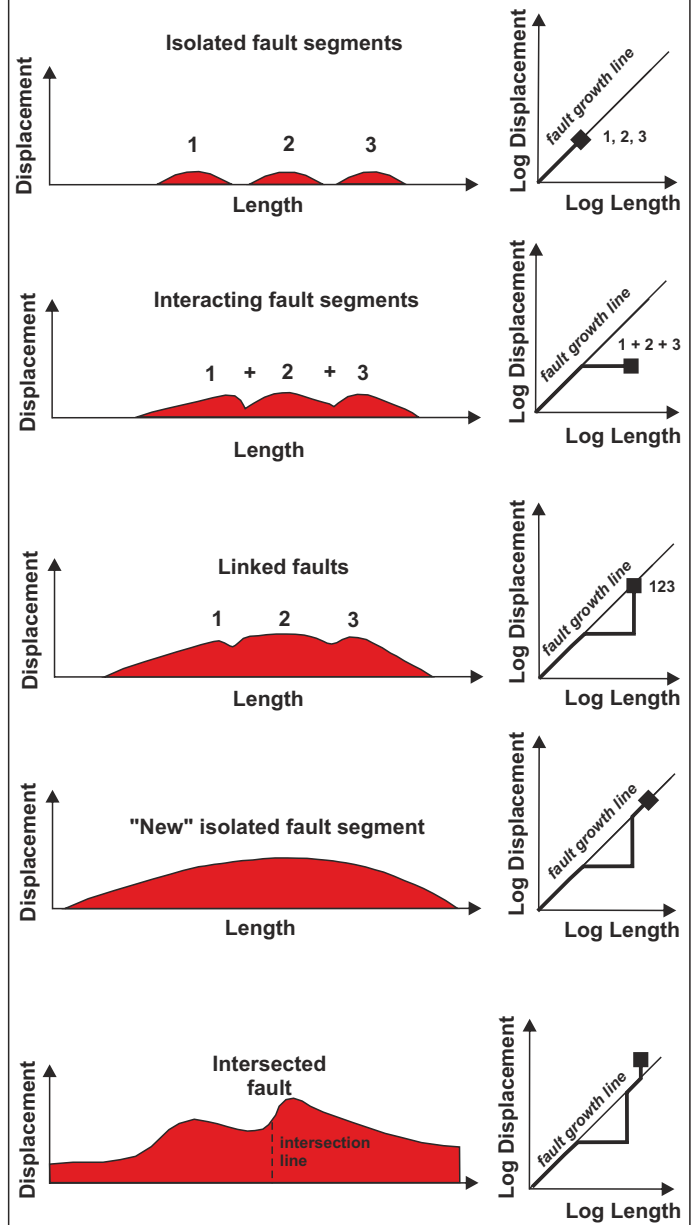


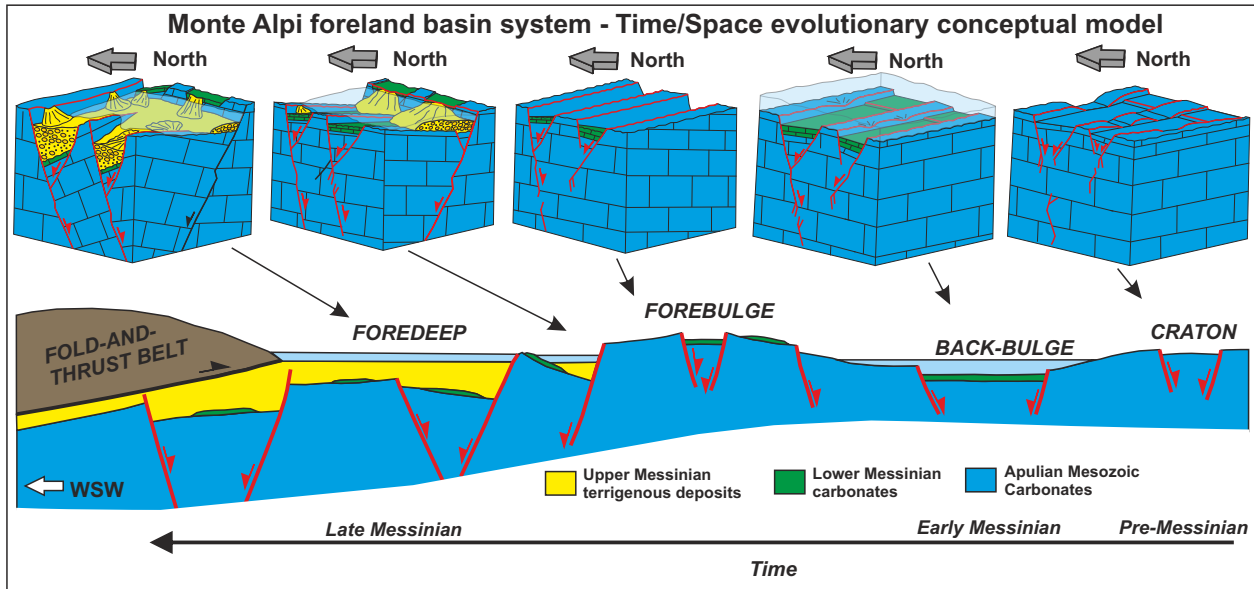
# PRE-MESSINIAN, EARLY-MESSINIAN AND POST-EARLY MESSINIAN THROW PROFILES





## Fault growth processes





**Highlights:**

- Both timing and growth processes are deciphered for the pre-Pliocene fault network;
- Main dimensional attributes computed for all analyzed faults;
- Inferences on the fault-control evolution of the Messinian foreland basin system;